

1 **Comparison of regolith physical and chemical characteristics with**
2 **geophysical data along a climate and ecological gradient, Chilean Coastal**
3 **Cordillera (26° to 38° S)**

Deleted: soil

Deleted: from

Deleted: and geochemical techniques

4
5 Mirjam Schaller^{1*}
6 Igor Dal Bo^{2*}
7 Todd A. Ehlers¹
8 Anja Klotzsche²
9 Reinhard Drews¹

10 Juan Pablo Fuentes Espoz³
11 Jan van der Kruk²

12
13 ¹ Department of Geosciences, University of Tübingen, Schnarrenbergstrasse 94-
14 96, 72076 Tübingen, Germany

Deleted: Germany,

15 ² Agrosphere (IBG-3), Institute of Bio- and Geosciences, Forschungszentrum
16 Jülich, 52428, Jülich, Germany

17 ³ University of Chile, Department of Silviculture and Nature Conservation, Av.
18 Santa Rosa 11315, La Pintana, Santiago RM, Chile

19 * Authors contributed equally.

20
21 Corresponding author: E-mail: Mirjam Schaller (mirjam.schaller@uni-
22 tuebingen.de)

23

24

29 **Abstract**

30 In this study, we combine geophysical observations from Ground Penetrating
31 Radar (GPR) with [regolith](#) physical, and [chemical](#) properties from pedons excavated
32 in four study areas spanning 1,300 km of the climate and ecological gradient in the
33 Chilean Coastal Cordillera. Our aims are to: (1) relate GPR observations to depth
34 varying [regolith](#) physical and weathering-related chemical properties in adjacent
35 pedons, and (2) evaluate the lateral extent to which these properties can be
36 extrapolated along a hillslope using GPR observations. Physical observations
37 considered include [regolith](#) bulk density and grain size distribution, whereas
38 chemical observations are based on major and trace element analysis. Results
39 indicate that visually-determined [pedolith](#) thickness and the transition from the B to
40 C horizons generally correlate with maximums in the 500 and 1000 MHz GPR
41 envelope profiles. To a lesser degree, these maximums in the GPR envelope
42 profiles agree with maximums in weathering related indices such as the Chemical
43 Index of Alteration (CIA) and the chemical index of mass transfer (τ) for Na. Finally,
44 we find that up-scaling from the pedon to hillslope scale is possible with geophysical
45 methods for certain pedon properties. Taken together, these findings suggest that
46 the GPR profiles [down](#) hillslopes can be used to infer lateral thickness variations in
47 [pedolith](#) horizons [in different ecologic and climate settings](#), and to some degree the
48 physical and chemical variations with depth.

49
50 Keywords: [regolith](#), [pedolith](#), hillslope, climate, vegetation, geophysics,
51

Deleted: soil

Deleted: geochemical

Deleted: soil

Deleted: soil

Deleted: soil

Deleted: soil

Deleted: available

Deleted: along

Deleted: soil

Deleted: soil, saprolite

62 **1 Introduction**

63 Weathering of bedrock by biotic and abiotic processes produces regolith which
64 provides resources for life. Most biota is found in the mobile pedolith, which overlies
65 the immobile saprolith. The pedolith is replenished with nutrients from the saprolith
66 through chemical weathering and erosion that drives nutrient uplift towards the
67 surface (e.g., Porder et al., 2007). The thickness and production of pedolith is
68 influenced by aspect, topography, composition (mineral content), biota, climate,
69 tectonically driven rock uplift, and time (e.g., Hilgard, 1914; Jenny, 1994). However,
70 subsurface variations in pedolith thickness at the scale of hillslopes are difficult to
71 quantify because of lack of exposure. Thus, subsurface imaging by geophysical
72 techniques, when calibrated to regolith excavations (pedons), offers a potential
73 mean to characterize spatial variability in pedolith thickness and regolith properties
74 (e.g., Mellett, 1995; Doolittle and Collins, 1995; Miller et al., 2004). Here, we
75 evaluate the utility of applying Ground Penetrating Radar (GPR) to map variations
76 in regolith properties caused by diverse climate and ecological settings.

77 Previous work has attributed spatial variations in pedolith thickness to hillslope
78 curvature (Heimsath et al., 1997; Heimsath et al., 1999), which determines the
79 downslope rate of mass transport assuming a diffusion-based geomorphic transport
80 law (e.g., Roering et al., 2001). However, this single point information is spatially
81 restricted and pedon excavations are time-intensive. To further understand spatial
82 variations in pedolith and saprolith thickness, other approaches such as modeling
83 (e.g., Scarpone et al., 2016) and geophysical imaging (e.g., see summary in
84 Parsekian et al., 2015) have been applied. For example, pedolith thickness
85 variations were extrapolated from Digital Elevation Models (DEMs) in combination
86 with several different observations at single locations (e.g., Scarpone et al., 2016).
87 Different geophysical techniques have provided a non- or minimally invasive
88 approach to view pedolith variations down to the saprolith and bedrock interface
89 (e.g., Parsekian et al., 2015). Whereas high frequency GPR has proven suitable for
90 investigating pedolith layering and thickness (e.g., Doolittle et al., 2007; Gerber et
91 al., 2010; Roering et al., 2010; Dal Bo et al., 2019), other methods such as seismics

Formatted: Normal, Justified, Indent: Left: -0", First line: 0"

Deleted: an upper

Deleted: layer (soil),

Deleted: is underlain by an

Deleted: layer of weathered material (saprolite) that replenishes the soil

Deleted: soil

Deleted: climate, biota, composition (mineral content),

Deleted: sub-surface

Deleted: soil

Deleted: soil pit

Deleted: one

Deleted: soil

Deleted: soil

Deleted: soil

Deleted: in

Deleted: with stark differences in physical and chemical soil properties

Deleted: soil

Deleted:

Deleted: soil

Deleted: saprolite

Deleted: soil

Deleted: soil

Deleted: saprolite

Deleted: soil

117 (e.g., Holbrook et al., 2014), Electrical Resistivity Tomography (ERT, e.g., Braun et
 118 al., 2009), and low frequency GPR (e.g., Aranha et al., 2002) are better suited to
 119 image [saprolith](#) and bedrock interfaces (e.g., Parsekian et al., 2015). GPR methods
 120 were [also](#) previously used to indirectly measure water flow (e.g., Zhang et al., 2014;
 121 Guo et al., 2020) as well as root density (e.g., Hruska et al., 1999; Guo et al., 2013).
 122 Interpreting the interplay of GPR signals with physical and chemical [regolith](#)
 123 properties is challenging (e.g., Saarenketo, [199](#); Sucre et al., 2011; Tosti et al.,
 124 2013; Sarkar et al., 2019).

125 The Chilean Coastal Cordillera (Fig. 1) contains an extreme climate and
 126 vegetation gradient and is a natural laboratory to study the influence of climate and
 127 vegetation on the surface of the Earth in a setting with similar tectonic history and
 128 lithology. The region is home to four study areas of the German-Chilean EarthShape
 129 priority program (www.earthshape.net), where investigations of biotic interactions
 130 with [regolith](#) are conducted (e.g., Bernhard et al., 2018; Oeser et al., 2018). The
 131 study areas were selected to [show a range from](#) arid climate in the northernmost
 132 location (26° S), [to](#) temperate rain forest conditions in the southernmost location
 133 (38° S). These four study areas are investigated to qualitatively and quantitatively
 134 describe the differences between the four settings. Our previous work in these areas
 135 has identified [from field observations and GPR based methods an increase](#) in
 136 [pedolith](#) thickness from north to south and major and trace element compositional
 137 variations within pedons (e.g., Bernhard et al., 2018; Oeser et al., 2018; Dal Bo et
 138 al., 2019). However, [in our previous GPR work \(Dal Bo et al., 2019\) we were not](#)
 139 [able to present](#) a detailed comparison of [physical, chemical, and regolith](#)
 140 observations [which has](#) yet to be [reported for](#) these areas.

141 In this [paper](#) we [build upon the previous work of Dal Bo et al. \(2019\) and compare](#)
 142 [the pedon measured](#) physical [and](#) chemical observations [\(from Bernhard et al.](#)
 143 [\(2018\) and Oeser et al. \(2018\)\)](#) to [newly acquired](#) GPR observations to gain insight
 144 into [regolith](#) variations [along a climate and ecological gradient](#). In general, we find
 145 that [our new](#) GPR [measurements](#) can be correlated to changes in [pedolith](#) physical
 146 properties if these changes are of sufficient magnitude and laterally coherent. If such

Deleted: saprolite

Deleted: also

Deleted: the distribution of

Deleted: soil

Deleted: within the sub-surface

Deleted: and not well-understood

Deleted: 1999

Deleted: it

Deleted: sub-

Deleted: a

Deleted: critical zone processes

Deleted: due

Deleted: the

Deleted: and

Deleted: both

Deleted: so far

Deleted: increases

Deleted: soil

Deleted: geophysical, geochemical

Deleted: soil

Deleted: is

Deleted: conducted in

Deleted: study,

Deleted: investigate how

Deleted: as well as

Deleted: measured at point locations (pedons) relate

Deleted: further

Deleted: the sub-surface

Deleted: .

Deleted: signals

Deleted: soil

178 a correlation is observed, we discuss the links between the physical and chemical
179 properties. The comparison of physical and chemical properties with field
180 observations and GPR data helps to better understand the regolith at point locations
181 (e.g., pedolith thickness) and in some cases allows for up-scaling point observations
182 to the hillslope scale along a GPR measurement profile.

Deleted: sub-surface

Deleted: soil

184 2 Study areas

185 Four primary study areas are investigated in the climatic and vegetation gradient
186 observed in the Chilean Coastal Cordillera (Figs 1 and 2; Table 2). From north to
187 south, the four selected areas are: a) Pan de Azúcar (~26.1° S); b) Santa Gracia
188 (~29.8° S); c) La Campana (~33.0° S); and d) Nahuelbuta (~37.8° S).

Deleted: Fig.

Deleted: N

Deleted: S

189 2.1 General climate, vegetation, and geologic setting

191 The Chilean Coastal Cordillera with its climate and vegetation gradient is a
192 natural laboratory to study the influence of climate and vegetation on denudation
193 (Fig. 1). From north to south (~26° to 38° S), present climate ranges from arid to
194 humid-temperate. The mean annual precipitation increases from nearly zero to
195 ~1500 mm yr⁻¹, and mean annual temperature decreases from ~20° C to ~5° C. The
196 flora consists of small shrubs, geophytes and annual plants (Armesto et al., 1993)
197 in the north and changes to lower-stature deciduous trees and shrubs intermix with
198 tall evergreen mixed forest in the south. Vegetation cover increases from nearly zero
199 to ~100%.

Deleted: N

Deleted: S

Deleted: close to

Deleted: N

Deleted: S

Deleted: close to

200 Climate and vegetation in the primary study areas changed over time from the
201 Last Glacial Maximum (LGM) to present. Mean annual precipitation during the LGM
202 was higher than at present in all four study areas (Mutz et al., 2018). Mean annual
203 temperature during the LGM was lower than at present except in the southernmost
204 study area where mean annual temperature stayed the same (Mutz et al., 2018).
205 Hence, the climate gradient observed today is comparable to the gradient during the
206 LGM. Even though the climate was wetter and cooler during the LGM, no glaciers

218 covered any of the study areas (Rabassa and Clapperton, 1990). Because of these
219 climatic changes over time, vegetation zones during the LGM were shifted
220 northward by ~5° and vegetation cover was slightly (~5-10%) lower compared to
221 present (Werner et al., 2018). This shift of vegetation zones to the north and the
222 decrease in vegetation cover also likely influenced the fauna present, but to an
223 unknown degree.

Deleted: Due to

Deleted: N

224 To compare the effect of climate and vegetation on pedolith thickness and GPR
225 observations, differences in lithologies need to be minimal. However, these
226 conditions are not always fulfilled and need to be taken in to account. Whereas
227 bedrocks in Pan de Azúcar, La Campana, and Nahuelbuta are granites to
228 granodiorites, the bedrocks in Santa Gracia range from Granodiorites to Gabbros
229 (Oeser et al., 2018). Hence, the parent material in Santa Gracia is lower in SiO₂-
230 content (50-65%) in comparison to the other three study areas (SiO₂-content >65%).
231 Chemical weathering and physical erosion, which in turn influence pedolith
232 formation and thickness, may be affected by this difference.

Deleted: soil

Deleted: the

Deleted: may be affected by this difference

Deleted: influences soil

234 2.2 Regolith Characteristics

Deleted: Soil

Deleted: depth

235 In each study area, regolith profiles from a catena consisting of three profiles on
236 the S-facing slope (top-slope, mid-slope, and toe-slope) and one profile on the N-
237 facing slope (mid-slope) were described, sampled, and analyzed (Fig. 3; see also
238 Bernhard et al., 2018; Oeser et al., 2018; Schaller et al., 2018; Dal Bo et al., 2019).

Deleted: soil

Deleted: (e.g., Bernhard et al., 2018)

Deleted: e.g.,

Deleted: .,

Deleted:).

Deleted: follow the approach of Riebe and Granger (2013) and ...

Deleted: soil layer

Deleted: saprolite layer represented by

Deleted:

Deleted: Azúcar

Deleted: soil is part of

Deleted: and

Deleted: thick A

Deleted: B

Deleted: .

239 Previous studies from pedons in each area identify O, A, B, and C horizons that
240 overlie weathered bedrock (for complete characterization and interpretation of the
241 pedons see Fig. 2 in Bernhard et al. (2018) and Figs 3 to 6 in Oeser et al. (2018).)
242 In this study, we refer to depth profiles as regolith profiles that are composed of a
243 mobile pedolith that includes the A and B horizons, and an immobile saprolith
244 including the C horizon.

245 In Pan de Azúcar, the regolith, a regosol (IUSS Working Group WRB, 2015),
246 consists of A and B horizons with a combined thickness of 20 to 25 cm and an
247 underlying saprolith (the C horizon), which is coarse-grained and jointed (Oeser et

272 [al., 2018](#)). The total organic carbon content [of the A and B horizons](#) is <0.1%
 273 (Bernhard [et al., 2018](#)). [Angular](#) fragments in the [pedolith](#) increase in size (> 1 mm)
 274 with depth. The average bulk density of the [A and B horizons](#) is 1.3 g cm⁻³. [In Santa](#)
 275 [Gracia, the 30 to 55 cm thick pedolith overlying the saprolite is a cambisol \(IUSS](#)
 276 [Working Group WRB, 2015\)](#). [Total organic carbon content of the A and B horizons](#)
 277 is 0.4%. Whereas the A horizon consists of a silt- to fine sand-sized matrix
 278 supporting up to 2 mm sized fragments, the underlying B horizon shows a
 279 transitional increase of fragments to a coarse fragment-supported fine-grained
 280 matrix. [The weathered granodiorite of the saprolite consists of up to 1 cm-sized](#)
 281 [fragments which are surrounded by fine-grained material and fine roots](#) (Oeser [et](#)
 282 [al., 2018](#)). The average bulk density [of the pedolith](#) is 1.5 g cm⁻³. The [regolith](#) in La
 283 [Campana is a cambisol \(IUSS Working Group WRB, 2015\)](#). [The A and B horizons](#)
 284 [are 35 to 60 cm thick and have a total organic carbon content of 1.9% \(Bernhard et](#)
 285 [al., 2018\)](#). The fine sand- to silt-sized A horizon contains fragments of up to 3 mm.
 286 The matrix in the underlying B horizon is coarsening downwards and the number of
 287 fragments increases such that the horizon shifts from matrix- to clast-supported. [In](#)
 288 [the saprolite, which shows a granodioritic fabric, fine roots are common and](#)
 289 [fractures are abundant \(Oeser et al., 2018\)](#). The average bulk density is 1.3 g cm⁻³.
 290 The [regolith](#) in Nahuelbuta, [an umbrisol \(IUSS Working Group WRB, 2015\)](#), consists
 291 of a 60 to 90 cm thick [pedolith](#) and a readily disaggregating [saprolite](#). [Total organic](#)
 292 [carbon content in these pedoliths](#) is 6.1% (Bernhard [et al., 2018](#)). The A horizon is
 293 composed of silt-sized particles forming nodular aggregates. In the upper part there
 294 are up to 1 mm large quartz grains embedded whereas the lower part contains large
 295 fragments. The fine sand-sized matrix of the transitional B horizon hosts subangular
 296 fragments. The amount and size of these fragments increases with depth. The
 297 average bulk density of the [pedolith](#) is 0.8 g cm⁻³.
 298

Deleted: la

Deleted: The observed angular

Deleted: soil

Deleted: The underlying saprolite is coarse-grained and jointed (Oeser et al., 2018).

Deleted: soil layer

Deleted: The cambisol in

Deleted: consists of

Deleted: layers of soil with A and B horizons

Deleted: saprolite (Bernhard et al., 2018). The total

Deleted: soils and saprolites

Deleted: form

Deleted: . The soil layers consisting of

Deleted: la

Deleted: umbrisol

Deleted: soil layer (A and B horizons)

Deleted: saprolite. The total

Deleted: soils

Deleted: la

Deleted: soil

Deleted: soil layer

320 **3 Data compilation and methods**

321 New data from 28 GPR profiles in the four study areas were collected at
322 frequencies of 500 and 1000 MHz. These data are compared to physical and
323 chemical properties from point locations (pedons) from previous studies (Bernhard
324 et al., 2018; Oeser et al., 2018). These new GPR profiles complement previous GPR
325 data collected at the same frequencies, in the same catchments (Dal Bo et al.,
326 2019). The difference between this study and that of Dal Bo et al. (2019) lies in the
327 new, more extensive, GPR data coverage and its comparison to physical and
328 chemical subsurface variations.

329 Using physical and chemical properties collected in pedons to understand the
330 corresponding radar signatures is a difficult task requiring multiple steps. First, it
331 would require identifying relationships between the measured pedon properties and
332 corresponding permittivity changes in the radar signal. Second, it would require a
333 radar forward model that successfully predicts the convolution of the emitted radar
334 pulse with the subsurface reflectivity. This includes handling constructive and
335 destructive interference caused by closely-spaced vertical permittivity changes. For
336 applications to regolith this is currently not possible because the permittivity
337 relationships are unclear. We therefore take a step back from the more
338 sophisticated methods, and use simpler statistical metrics to isolate regolith
339 properties (i.e. Pearson correlation) or combinations thereof (i.e. Principal
340 Component Analysis) that may explain parts of the radar signatures.

341
342 3.1 Data compilation

343 In this study, GPR data are compared to previously published pedolith and
344 saprolite physical and chemical properties (Table 1) such as: 1) bulk density, grain
345 size distribution, pH, and cation exchange capacity - CEC (Bernhard et al., 2018);
346 and 2) Loss On Ignition - LOI, Chemical index of Alteration - CIA, mass transfer
347 coefficient τ , and volumetric strain, ϵ_{strain} (Oeser et al., 2018). The grain size
348 distributions provide a measure of the weight percent of different grain sizes smaller
349 than 2 mm in the regolith, and the bulk density provides a measure of how dense

Deleted: 32

Deleted: the
Deleted: of it

Deleted: and physical

Deleted: treatment on

Deleted: layers

Deleted: need fixed

Deleted: translating

Deleted: to

Deleted: relevant for

Deleted: need

Deleted: sub-surface

Deleted: among others

Deleted: in the vertical.

Deleted: on soil,

Deleted: already

Deleted: trying

Deleted: some

Deleted: soil

Deleted: saprolite

Deleted: soil

Deleted: regolith

372 the [pedolith](#) and [saprolith](#) material is packed. The geochemical data used provide
373 major and trace element analysis, the acid and base properties (pH) and cation
374 exchange capacity (CEC). Major and trace element [analyses](#) allow the investigation
375 of the loss on ignition (LOI), the chemical index of the mass transfer coefficient (τ),
376 and the volumetric strain (ϵ_{strain}). LOI is a measure of the loss of volatile substances
377 in a material due to excess heating (1000°C), thereby reflecting the amount of
378 [organic matter in regolith](#). The degree of weathering can be quantified by the CIA
379 which is sensitive to the removal of alkalis such as calcium, sodium, and potassium
380 from feldspars (Nesbitt and Young, 1982). The mass transfer coefficient (τ_{strain})
381 reflects chemical gains and losses during weathering based on the elemental
382 concentrations of mobile and immobile elements in weathered and unweathered
383 material (e.g., Brimhall et al., 1985; Chadwick et al., 1990), ϵ_{strain} in a regolith is
384 based on the density ρ (g cm^{-3}) and immobile element concentrations of the
385 weathered regolith in comparison to the unweathered bedrock indicating volumetric
386 gain or loss (Brimhall and Dietrich, 1987).

Deleted: soil

Deleted: saprolite

Deleted: analysis

Deleted: soil

387 [Finally, although GPR signals can be sensitive to regolith moisture content](#)
388 [variations with depth \(e.g., Steelman et al., 2012; Ardekani et al., 2014\), regolith](#)
389 [moisture measurements were not conducted in the pedons. As such, these](#)
390 [measurements do not appear in Bernhard et al. \(2018\) or Oeser et al. \(2018\) and](#)
391 [are not available for comparison to the measured GPR signals. Furthermore, the](#)
392 [GPR data were not collected in an approach that allowed for the inversion of regolith](#)
393 [moisture content \(e.g., Steelman et al., 2012\). The pedons sampled in Bernhard et](#)
394 [al. \(2018\) and Oeser et al. \(2018\) were excavated in early 2016 and promptly refilled](#)
395 [due to their locations in national parks and a nature preserve. The GPR data](#)
396 [presented in this study were collected in 2017 and no resampling of the pedons for](#)
397 [regolith moisture was possible. As a result, some of the unexplained signal in our](#)
398 [GPR data may result from the omission of regolith moisture in our analysis.](#)

399

400 3.2 Ground Penetrating Radar (GPR)

405 Ground Penetrating Radar (GPR) is a geophysical technique based on the
 406 emission of pulsed electromagnetic waves into the subsurface. In this study,
 407 frequencies of 500 and 1000 MHz are used. The electromagnetic waves are
 408 reflected and scattered in the presence of dielectric contrasts at depth. The back-
 409 propagated reflected wave is then received as travel times, which depend on the
 410 depth-variable electromagnetic wave velocity v . The velocity of the media is dictated
 411 by the relative dielectric permittivity ϵ_r (Jol, 2009). Attenuation of the waves can be
 412 linked to the electrical conductivity σ . Vertical resolution depends on the system's
 413 bandwidth and the wave velocity and is in our case approximately 0.07 m for 500
 414 MHz and 0.03 m for 1000 MHz. Surface GPR can be measured in two ways
 415 including: 1) Common-Offset Profiling (COP) and 2) Common-midpoint (CMP) or
 416 wide-angle-reflection-refraction (WARR) measurements (see also Dal Bo et al.,
 417 2019). COPs measure traveltimes versus spatial position along specific transects
 418 with two antennae at fixed offsets. Here, this was done along profiles crossing the
 419 pedons (e.g., Figs 2 and 3). WARRs are used to retrieve velocity and physical
 420 properties at the point scale with variable antennae spacing. Specifically, for each
 421 pedon a WARR was measured in a relatively flat location by keeping the transmitter
 422 position fixed at the pedon location and by moving the receiver towards the
 423 transmitter with in steps varying between 0.01 and 0.05 m depending on the
 424 deployed frequency. Using this type of survey, we can distinguish between signals
 425 that increase linearly in traveltimes with increasing receiver-transmitter distance (e.g.,
 426 air wave and ground wave) and signals that increase hyperbolically in traveltimes
 427 with increasing receiver-transmitter distance (e.g., subsurface reflections). In this
 428 analysis, we assume that internal reflection horizons are not dipping.
 429 Twenty-eight COP transects going from hillslope toe (near valley) to top (ridge
 430 crest) were collected in the four study areas using 500 and 1000 MHz GPR
 431 antennae (Sensor and Software Inc.). The average trace spacing of these vary
 432 between 0.01 and 0.05 m depending on frequency and location. These transects
 433 were chosen to run between pedons, where physical and chemical properties were
 434 collected (Bernhard et al., 2018; Oeser et al., 2018). Of these 28 profiles, two were

Deleted: and here

Deleted: applied

Deleted: at

Deleted: The attenuation

Deleted: The vertical

Deleted: refractions

Deleted: Fig.

Deleted: a step size

Deleted: In such way, the move-outs

Formatted: Font color: Text 1

Deleted: linear events (

Formatted: Font color: Text 1

Deleted: of hyperbolic events (sub-surface

Formatted: Font color: Text 1

Deleted:) could be identified using the underlying assumption...

Formatted: Font color: Text 1

Deleted: reflectors

Formatted: Font color: Text 1

Deleted: in such a way as

Deleted: the previously described

451 collected in the Pan de Azúcar study area, six in Santa Gracia, three in La Campana,
452 and three in Nahuelbuta. Each profile was measured twice (at the two frequencies)
453 [to total 28](#). The pedon locations formed the basis for comparison to the GPR data
454 as ground-truth data and WARRs and COPs where collected specifically at these
455 positions (red stars, Fig. 2). Additionally, four perpendicular GPR crosslines
456 (perpendicular to the transects) were measured at both the 500 and 1000 MHz in
457 the La Campana and Nahuelbuta study areas. The position of each profile was
458 determined using a differential GPS (Leica Geosystems AG) with a maximum
459 horizontal and vertical precisions of 2 and 4 cm, respectively.

Deleted: to total 28

Deleted:).

460 GPR data were processed and analyzed similar to Dal Bo et al. (2019) using
461 MATLAB. The GPR data processing procedure included: frequency band-pass filter,
462 amplitude gain, background removal, and time-to-depth conversion (e.g., Jol, 2009).
463 The direct air wave between receiver and transmitter was muted. Similar to Dal Bo
464 et al. (2019), the newly measured WARR profiles at the pedon locations were
465 processed and analyzed using a combined linear [moveout](#) – hyperbolic [moveout](#)
466 approach (Dal Bo et al., 2019). Ground wave and reflection velocities were picked,
467 from which an average value of GPR velocity per each study area was derived and
468 used for the time-to-depth conversion of the COP profiles (see [approach of](#) Dal Bo
469 et al., 2019). The averaged value of GPR velocities is used to study [pedolith](#) depths
470 on [a](#) hillslope scale. However, the use of an average will result in an over-/under-
471 estimate of [pedolith](#) depths [at](#) the hillslope scale. Signal envelopes were calculated
472 using a Hilbert transform (Green, 2004; Liu and Marfurt, 2007). At each pedon
473 location, a certain number of traces depending on the measurement step size (i.e.
474 between 10 and 50) were sampled for 0.5 m uphill and 0.5 m downhill the pedon
475 and laterally averaged for comparison to the pedon physical and chemical
476 properties. The averaging assumes that both chemical and GPR signatures do not
477 change with depth across that interval, an assumption that may not hold
478 everywhere. As the GPR envelope is directly related to the electric impedance
479 (Telford et al., 1990; Jol, 2009), the envelope onset and energy intervals could be
480 compared to variations in physical, and potentially chemical, [regolith](#) properties.

Deleted: move-out

Deleted: move-out

Deleted: .

Deleted: soil

Deleted: soil

Deleted: on

Deleted: soil

490
491
492
493
494
495
496
497
498
499
500
501
502
503
504
505
506
507
508
509
510
511
512
513
514
515
516
517
518
519

3.3 Statistical Correlation and Principal Component Analysis

Comparison between the [physical and chemical](#) pedon information (Bernhard et al., 2018; Oeser et al., 2018) and GPR data was conducted [in two ways](#). First, we carried out a correlation analysis using the Pearson' correlation coefficient (r). More specifically, we used the bulk density, clay content, LOI, CIA, Tau (τ), volumetric strain (ϵ_{strain}), pH, and CEC for comparison to the GPR 500 and 1000 MHz antennae envelope data. The GPR envelopes were resampled and averaged, such that the depth intervals were the same as for the derivatives of the [regolith](#) data (see Table S2). Furthermore, because the envelope of GPR data is sensitive to changes along the vertical direction, we also calculated the vertical gradient of the ground truth information at each sampled depth using a centered difference approximation. Following this, the R package function corplot (Wei, 2012) was used to calculate the Pearson's correlation coefficient to identify correlations between the variables (Sedgwick, 2012). This analysis was [carried out for](#) the entire climate and vegetation gradient and [for](#) each location. Both the original data and the derivatives were used to explore which of the two approaches delivered meaningful insights.

Second, we conducted a multivariate analysis of the data using a principal component analysis (PCA; Wold et al., 1987). This was done for both the entire climate gradient and [for](#) each study area using the factoextra R package (Kassambara, 2017). After each PCA analysis, a scree plot was evaluated to investigate how much variance was included in each principal component (PC; Bro and Smilde, 2014). In this study, at least 70% of the variance was [in](#) the first two PCs, which were then further analyzed. The contribution of each variable to the first and second PC was computed using the eigenvalues and eigenvectors from the covariance matrix (Abdi and Williams, 2010). This resulted in a plot where the x-axis is PC1 and the y-axis is PC2 and each variable is displayed as a vector with a specific direction and length that indicate the magnitude and direction of the contribution to each PC.

Deleted: and physical

Deleted: different

Deleted: soil

Deleted: done considering

Deleted: within

Deleted: within

Deleted: ,

Deleted: among

528 **4 Results**

529 Physical and chemical properties of pedons are shown with the 500 and 1000
530 MHz GPR profiles and their envelopes with depth as well as investigated
531 correlations and PCAs for the four study areas (Figs 4 to 11; Figs S1 to S12; Tables
532 S1A to D, S2A to D, S3, and S4A to E). For brevity, comparisons between pedon
533 observations and GPR data are presented only for the S-facing mid-slope positions
534 in the main text (Figs 4, 6, 8, and 10) and the remaining locations are provided in
535 the supplementary material. Note that the envelopes are averaged over the COP
536 data, collected over a lateral distance of 1 m in total, and are therefore not point
537 information. Given that the pedolith thickness increases towards the southern study
538 areas, the 1000 MHz GPR antenna is interpreted for the northern two study areas
539 Pan de Azúcar and Santa Gracia, whereas in La Campana and Nahuelbuta the 500
540 MHz GPR signal was used because it has a deeper penetration depth. However,
541 we show results below for both frequency antennas to demonstrate the difference
542 in penetration depth and resolution between the two antennae. Details for each
543 study area (from north to south) follow.

545 4.1 Pan de Azúcar (northern most study area)

546 In Pan de Azúcar (Figs 1, and 2A), a gradual transition from the B to the C horizon
547 was visually observed in the pedons at 20 to 40 cm (shaded gray areas after
548 Bernhard et al. (2018); Fig. 4; Figs S1 to S3), whereas the mobile, and immobile
549 boundary is considered to be at 20 to 25 cm (black lines after Oeser et al., (2018);
550 Fig. 4; Figs S1 to S3). The available physical properties for this location do not
551 indicate a strong change in material properties with depth. LOI and CIA indicate a
552 minor change in properties at ~20 cm depth. A maximum in the energy envelope in
553 the 1000 MHz frequency is present at about 20 to 30 cm, and could be related to
554 the transition of material properties between the B and C horizons and the location
555 of mobile, and immobile boundary observed in the field.

556 Due to the sparse depth information for bulk density and clay content, the
557 statistical analyses for this location were not very insightful. Whereas clay content

Deleted: from

Deleted: Fig.

Deleted: and supplement

Deleted: and supplement

Deleted: only the

Deleted: Fig.

Deleted: soil

Deleted: antennae

Deleted: (

Deleted:)

Deleted: study areas

Deleted: N

Deleted: S

Moved down [1]: Fig.

Deleted: ,

Deleted: /

Deleted: (shaded gray areas and

Deleted: line, Fig. 4,

Deleted: that

Deleted: /

Deleted: was

579 shows a medium correlation (0.54) with the 1000 MHz GPR envelope, no strong
580 correlation between LOI, CIA, τ , and the 1000 MHz GPR envelope could be found
581 (Table S3). In the PCA, three primary components (PC) explain over 80% of the
582 variance (Table S4A). PC1 has the biggest contribution from CIA, clay content, and
583 the 500 MHz envelope whereas PC2 has the biggest contribution from LOI, the
584 1000MHz envelope, and τ of Na and Zr (Fig. 5).

Deleted: bigger

Deleted: bigger

585 586 4.2 Santa Gracia

587 In Santa Gracia (Figs 1, and 2B), a gradual transition from the B to the C horizon
588 was observed in the field between 20 to 60 cm depth (shaded gray region Fig. 6;
589 Figs S4 to S6). The boundaries between the pedolith and saprolith were observed
590 between 30 to 55 cm depth. Bulk density and volumetric strain show slight changes
591 around 15 and 30 cm depth. Whereas LOI and CIA do not show any changes with
592 depth, τ shows changes between 30 and 50 cm depth. The 500 and 1000 MHz GPR
593 profiles and envelopes show increased irregular and strong reflections at ~25 cm
594 (1000 MHz) and 45 cm (500 MHz) depth, and also maximums in the envelope at
595 ~25 cm (1000 MHz) and 45 cm (500 MHz) depths. These variations in the reflections
596 and maximums in the envelopes coincide with either the top or central position of
597 the transition from the B to the C horizon.

Deleted: Fig.

Deleted: ,

Deleted: , Fig.

Deleted: mobile/immobile layers in the pedon

598 A weak to moderate correlation (~0.3) between clay content as well as CIA and
599 the 1000 MHz GPR envelope is present (Table S3). Results from a PCA analysis of
600 the Santa Gracia data indicate that 3 components explain over 80% of the observed
601 variance (Table S4B). PC1 explains over 35% of the variance, and includes bulk
602 density, CIA, and the 500 and 1000 MHz envelopes (Fig. 7). PC2, explaining 31%
603 of the variance, includes clay content, LOI, and τ of Na and Zr.

604 605 4.3 La Campana

606 Field observations from the La Campana area (Figs 1, and 2C) document a layer
607 of cobbles (5 to 10 cm diameter) between the A and B horizon at a depth of ~30 cm

Deleted: Fig.

Deleted: ,

616 (Bernhard et al., 2018). The transition between the B to C horizons does not contain
617 rock fragments. The transition from the B to C horizon (shaded gray area, Fig. 8)
618 and the mobile and immobile boundary (black line, Fig. 8) are observed at 34 to 110
619 cm and 35 to 60 cm, respectively (see also Figs S7 to S9). The pedolith extends
620 deeper in La Campana than in Pan de Azúcar or Santa Gracia and physical
621 properties were available for greater depths. Bulk density and grain size change
622 gradually with depth and no pedolith thickness could be determined. Also, LOI, CIA,
623 and τ do not show an abrupt change in regolith properties. Reflection hyperbolas
624 and irregular reflection horizons appear in the 500 and 1000 MHz GPR data at about
625 40 to 60 cm depth above the B to C horizon transition. The second peaks of the 500
626 and 1000 MHz GPR envelopes coincide with the B to C horizon transition.

627 In contrast to the previous study areas, the 500 MHz GPR envelope correlates
628 moderately with CIA (0.56), pH (-0.57), and CEC (-0.39, Table S3). Three
629 components from the PCA analysis explain about 80% of the total variance (Table
630 S4C). PC1 (~35% of the total variance) includes LOI, τ , and CEC, whereas PC2
631 (31%) contains CIA, volumetric strain ϵ_{strain} , and the envelopes (Fig. 9). PC3 is
632 dominated by pH as well as τ of Zr. In general, whereas the first energy interval
633 (1000 MHz) could be attributed to the stone layer between the A and B horizon, the
634 second energy interval occurs close to (<10 cm) with the mobile and immobile
635 boundary (Fig. 8).

636 637 4.4 Nahuelbuta (southernmost study area)

638 In Nahuelbuta, the B horizon contains pebbles and cobbles at around 60 to 80
639 cm depth (Bernhard et al., 2018). The B to C horizon transition appears at 50 to 100
640 cm depth (shaded gray region, Fig. 10; see also Figs S10 to S12). The mobile and
641 immobile boundary was identified at 60 to 90 cm depth (Oeser et al., 2018). Density
642 measurements in the pedon indicate a transition in bulk density between about 30
643 to 60 cm depth where the grain size distribution also changes. The LOI and τ
644 generally show large changes with depth, in contrast to the CIA and volumetric strain

Deleted: /

Deleted: Fig.

Deleted: mobile soil layer

Deleted: soil

Deleted: /

Deleted: Fig.

Deleted: /

Deleted: .

Deleted: also

654 which are more homogenous with depth. The 500 MHz GPR profile indicate the
655 existence of point targets/objects appearing as reflection hyperbola or undulating
656 features at depths greater than 60 cm. This depth is approximately the same depth
657 at which the mobile, and immobile boundary was identified, as well as changes in
658 the physical properties (e.g. bulk density, percent sand) and chemical properties
659 (LOI, τ). The hyperbolas do not add up coherently during the lateral averaging and
660 therefore do not produce a significant energy interval in the average envelope. The
661 envelope is dominated by the energy intervals given by two reflections at about 30
662 to 50 cm depth. The lower set of these energy intervals could be linked with the
663 upper physical pedolith boundary.

Deleted: 60cm

Deleted: /

Deleted: τ properties.

Deleted: soil

664 Results from the correlation analysis indicate that the 500 MHz GPR envelope
665 is strongly positively correlated with bulk density (0.74), strongly inversely correlated
666 with LOI (-0.60), and moderately inversely or positively correlated with clay content
667 (-0.37), pH (0.46), and CEC (-0.53) (Table S3). Results from the PCA analysis show
668 that two PC components explain ~75% of the variance. PC1 (~57 %) includes bulk
669 density, clay content, LOI, and CEC, and PC2 (~18 %) contains τ of Zr and pH (Fig.
670 11; Table S4D). In general, as the 500 MHz GPR envelope signal correlates well
671 with bulk density and clay content, the envelope signal reflects changes in regolith
672 properties.

Deleted: 6

Deleted: whereas

Deleted: soil

674 **5 Discussion**

675 Here we evaluate the physical, chemical, and geophysical observations from the
676 pedons. Using this information, we attempt to up-scale information from the pedons
677 to the hillslopes scale along the GPR transects. Potential pedolith thickness over
678 hillslopes is discussed in light of hillslope, aspect, and the climate and vegetation
679 gradient from north to south.

Deleted: , physical

Deleted: soil

Deleted: N

Deleted: S

681 **5.1 Synthesis of GPR data with physical and chemical properties from point** 682 **locations**

694 GPR data image [subsurface](#) changes that could be caused by [variations](#) in
695 physical (e.g., bulk density, grain size variation, water content), or potentially
696 chemical properties (e.g., pH, CEC, CIA). The interplay between these different
697 properties can have a complicated influence on the GPR signal and therefore [can](#)
698 [be](#) difficult to disentangle. Disentangling any relationship between GPR data and
699 physical and chemical properties is further complicated [because](#) not all properties
700 influencing GPR data are measured (e.g., water content; Jol, 2009). In addition, the
701 determination of the boundary between the [pedolith and saprolith](#) in the field causes
702 its own problems [because](#) observed changes are [not discrete but](#) transitional over
703 a depth interval of 5 to 10 cm. In the following, we start by discussing if GPR data
704 can be used to image [pedolith](#) thickness as well as physical and chemical properties
705 at the pedon locations where *in-situ* observations were made in each study area.

706 In Pan de Azúcar ([Figs 4 and 5; Figs S1 to S3](#)), the locations where GPR data
707 can be compared to pedons [show](#) low variability in the observed [pedolith](#) thickness
708 (~20 to 30 cm) at each pedon location. Whereas the 500 MHz signal shows [the](#)
709 [interface with the saprolith](#), the maximum in the 1000 MHz energy interval signal
710 agrees with the [pedolith](#) thicknesses observed in the field (Fig. 4 and [Figs S1 to S3](#)).
711 However, the boundary between [the pedolith and saprolith](#) is probably too shallow
712 to be detected with the 1000 MHz [antenna](#). An even higher frequency would be
713 [required](#) to detect the [pedolith and saprolith](#) boundary. Hence the Pearson
714 correlations and PCA results from Pan de Azúcar are restricted not only because of
715 GPR analysis but also due to restricted physical properties. The [physical and](#)
716 [chemical](#) properties correlate only weakly to moderately with the 1000 MHz
717 envelopes (Table S3). The PCA results indicate that [bulk density](#) is not likely
718 correlated with either the 1000 MHz signal or LOI. In Pan de Azúcar, LOI does not
719 represent [organic matter](#) [because regoliths](#) of arid zones [generally](#) have low or no
720 organic matter content. The volatile loss measured in the LOI is more likely
721 associated with the combustion of carbonates. In general, shallow [pedoliths](#) in the
722 arid zone do not show much variability in [pedolith](#) thickness nor [do they](#) provide
723 insight into the influence of physical or chemical properties on GPR signals.

Deleted: in material properties

Deleted: changes

Deleted: as

Deleted: soil thickness (i.e.,

Deleted: mobile/immobile layers)

Deleted: as

Deleted: and not discrete.

Deleted: soil

Deleted: Fig.

Deleted: , 5

Deleted: Fig.

Deleted: shows

Deleted: soil

Deleted: deep (sub-soil depth) interfaces

Deleted: soil

Formatted: English (UK)

Deleted: Fig.

Formatted: English (UK)

Deleted: soil

Deleted: saprolite layers

Deleted: here

Deleted: antennae

Deleted: favourable

Deleted: soil/saprolite

Deleted: and physical

Formatted: Font color: Text 1, English (UK)

Deleted: soil

Deleted: soil

Deleted: as soils

Deleted: the

Deleted: soils

Deleted: soil

753 In Santa Gracia (Figs 6, and 7; Figs S4 to S6), the field-observed pedolith
754 thicknesses of the different pedons are more variable than in Pan de Azúcar.
755 Although the 500 MHz and 1000 MHz GPR envelopes indicate changes at depth,
756 the physical and chemical properties observed with depth show only a few distinct
757 changes implying that the pedolith thickness cannot easily be determined using only
758 physical or chemical properties. The PCA indicates that most of the variance in PC1
759 is explained by the envelope signals, bulk density, and CIA whereas PC2 is
760 dominated by clay content and τ of Na and Zr. The clay content does not seem to
761 be a dominant factor for the envelope signal, but rather represents a complex
762 interaction between physical and chemical property changes that cannot be
763 disentangled with available data. It appears that the second energy interval in the
764 1000 MHz envelope may agree with the observed pedolith thickness in Santa
765 Gracia, and (in contrast to the Pan de Azúcar location) the first maximum in the 500
766 MHz envelope does agree with the observed pedolith thickness. These
767 observations again underscore, that for different locations with variable regolith
768 type, vegetation, and physical and chemical properties local calibration between
769 pedons and GPR data are required.

770 The determination of pedolith thickness from GPR data in La Campana is as
771 difficult as in the previous settings (Figs 8, and 9; Figs S7 to S9). Field observations
772 indicate relatively thick transition zones from the B to C horizons, and some physical
773 properties vary only weakly with depth. As a result, the determination of pedolith
774 thickness with physical and chemical properties is difficult, despite the moderate to
775 strong correlation of 500 MHz GPR envelopes with derivatives of physical and
776 chemical properties. Whereas the variance in PC1 is explained by bulk density, LOI,
777 τ of Na and Zr, and volumetric strain, the variance in PC2 is dominated by the
778 envelopes, CIA, pH, and CEC. Chemical properties seem to have a considerable
779 influence on GPR signals in this setting. In La Campana, the first energy interval in
780 the 500 MHz envelope is interpreted to reflect the presence of the stone layer
781 whereas the second energy interval seems to match the observed pedolith

- Deleted: Fig.
- Deleted: , 7
- Deleted: Fig.
- Deleted: soil

Deleted: soil

Deleted: soil

Deleted: soil

Deleted: soil

Deleted: soil

Deleted: Fig.

Deleted: , 9

Deleted: Fig.

Deleted: The field

Deleted: large

Deleted: for

Deleted: the

Deleted: horizon

Deleted: soil

Deleted: of

Deleted: previously described

Deleted: soil

803 thickness. Given these uncertainties in local conditions, a clear identification of
804 pedolith thickness from GPR data is difficult, even with local calibration to a pedon.

805 Finally, in Nahuelbuta (Figs 10 and 11: Figs S10 to S12), the observed pedolith
806 thickness in the field is the deepest of all the four study areas and reaches from 50
807 to 100 cm. The pedolith thickness is easily identifiable based on physical properties,
808 (e.g., bulk density, grain size variation). The derivatives of the physical properties
809 correlate moderately with the available 500 MHz envelope (Table 3). Furthermore,
810 the chemical properties correlate weakly with the GPR envelope. The variance is
811 strongly explained by PC1 containing physical properties (e.g., bulk density, clay
812 content, LOI) and less by PC2 including chemical properties (e.g., pH, τ of Na and
813 Zr). Even though changes in properties are more pronounced in Nahuelbuta than in
814 the drier locations, a clear correlation between maximums in the 500 MHz energy
815 envelope and pedolith thickness is not present. The second energy interval of the
816 500 MHz envelope best agrees with the observed pedolith thickness. However, due
817 to local inhomogeneities caused by intense vegetation, every pedon and its
818 attributed GPR envelope looks different.

819 In summary, the 500 and 1000 MHz envelopes at point locations have the
820 potential to be used to determine pedolith thickness. But the clarity with which this
821 can be done is variable and requires calibration to local pedons. Even with local
822 calibration, the relationships are not always clear (e.g., Fig. 8). Physical and
823 chemical properties with depth exert a complex influence on measured GPR signals.
824 If a certain combination of physical and chemical properties is dominant in one
825 setting, another combination may influence the measured GPR signal. Therefore,
826 which GPR frequency works best for the individual study area (due to different
827 physical and chemical properties) needs to be investigated with information from
828 point locations/pedons. For the arid Pan de Azúcar and semi-arid Santa Gracia we
829 suggest using the 1000 MHz frequency (or higher), whereas for the Mediterranean
830 climate setting of La Campana and temperate Nahuelbuta the 500 MHz frequency
831 proved better. Improvements in our approach to determine pedolith thickness from
832 GPR data might be possible by applying multifrequency GPR techniques, which are

Deleted: soil

Deleted: Fig.

Deleted: , 11

Deleted: Fig.

Deleted: soil

Deleted: soil

Deleted: .

Deleted: envelops

Deleted: so

Deleted: soil

Deleted: soil

Deleted: look

Deleted: soil

Deleted: .

Deleted: interplay

Deleted: what

Deleted: soil

850 freed from antenna effects by fusion of different frequency measurements (e.g., De
851 Coster and Lambot, 2018). Nevertheless, the point information of [pedolith](#) thickness
852 has the potential to be up-scaled to hillslopes in some settings using GPR transects
853 after local calibration is conducted.

Deleted: soil

854

855 5.2 Up-scaling to hillslopes

856 Here we use insights gained from comparisons between GPR and point
857 locations to extrapolate the [pedolith](#) thickness along the hillslope GPR profiles ([Figs](#)
858 [2 and 3](#)). [Our efforts here complement previous work by Dal Bo et al., \(2019\) by](#)
859 [adding 28 new GPR profiles that cover a larger geographic region.](#) The up-scaling
860 is carried out using a combination of amplitude and envelope depth-converted
861 profiles. To do this up-scaling, we calculated the envelope along each profile. Then,
862 using the known [pedolith](#) depth data from all pedons in one study area, this interface
863 was estimated along the profiles by searching for the corresponding signal in the
864 envelope at every meter. Even though the information of three-point locations is at
865 the lower limit, the combination of field observations with GPR transects allows
866 estimation of the lateral variability of [pedolith](#) thickness over hillslopes. However, the
867 complications [which frequency of GPR antenna to use for analysis \(Dal Bo et al.,](#)
868 [2019\) in addition to what](#) envelope interval to [select \(section 5.1\) requires careful](#)
869 up-scaling [of the pedolith thickness to hillslopes.](#)

Deleted: soil

Deleted: Fig.

Deleted: ,

Deleted: soil

Deleted: soil

Deleted: given

Deleted: mentioned in section 5.1 (e.g.,

Deleted: and

Deleted: use) the

Deleted: and

Deleted: indicated soil

Deleted: need to be treated with care

Deleted: Supplementary

Deleted: soil

Deleted: soil

870 In Pan de Azúcar (Fig. 12; Fig. S14) the observed B to C horizon transition at
871 point locations is typically between ~14 to 50 cm. No clear [pedolith](#) thickness could
872 be determined based on GPR profiles. Nevertheless, [pedolith](#) thicknesses identified
873 from 1000 MHz GPR envelopes seem to be relatively homogeneous over the entire
874 S-facing transect with an average value of 25 ± 3 cm (Table 2). In contrast, the N-
875 facing transect indicates a thinner [pedolith](#) uphill than downhill where it reaches a
876 maximum depth of ~50 cm (Fig. S14).

Deleted: soil

877 In Santa Gracia (Fig. 13; [Figs S15 to 17](#)), the [pedolith](#) thicknesses from point
878 locations/pedons in the S-facing transect increases downslope and ranges between
879 20 to 60 cm (Table 2). The [pedolith](#) thickness based on the 1000 MHz GPR

Deleted: Supplementary Fig.

Deleted: soil

Deleted: soil

900 envelope at the top-slope position (SGPED20) decreases first downhill and then
901 increases again, thereby demonstrating laterally variability [down](#) the hillslope. The
902 [pedolith](#) thickness in the mid-slope position (SGPED40) is variable and reaches
903 from 25 to 50 cm. At the toe-slope position (SGPED60) a mostly constant thickness
904 of 30 cm is identified. In the N-facing transect almost no variability in [pedolith](#)
905 thickness (~25 cm) is observed. [Although](#) the [pedolith](#) thickness based on GPR
906 envelopes cannot be used to decipher the exact [pedolith](#) thickness, the method still
907 offers a close approximation of [pedolith](#) thicknesses determined by field
908 observations and GPR profiles.

909 In La Campana (Fig. 14; [Figs](#) S18 to 20) the [pedolith](#) thickness from the 500
910 MHz GPR envelope is 35 to 70 cm. Whereas the top- and mid-slope positions in the
911 S-facing hillslope (LCPED10 and LCPED20, respectively) show variable [pedolith](#)
912 thickness between 50 and 70 cm, the toe-slope position (LCPED30) contains
913 [pedolith](#) thicknesses between 35 and 70 cm. Relatively constant [pedolith](#) thickness
914 of 50 to 60 cm are identified for the N-facing mid-slope position (LCPED40). Field
915 observations do not always agree with [pedolith](#) thicknesses based on GPR
916 envelopes. In the La Campana location, [pedolith](#) thicknesses based on GPR
917 envelopes need to be considered with caution, but contain valuable information such
918 as the existence of pebble layers. However, GPR profiles show hyperbolas and
919 continuous reflections, which can be interpreted along almost all the covered length.
920 These interfaces can be reliably used to infer [pedolith](#) thicknesses, when a previous
921 calibration with [pedons](#) has been done.

922 In Nahuelbuta (Fig. 15; [Figs](#) S21 to 23), [pedolith](#) thickness in the S-facing top-
923 slope position (NAPED10) increase downhill from 60 to 110 cm. At the mid-slope
924 position (NAPED20), the [pedolith](#) thickness is highly variable and ranges from 50 to
925 110 cm. [Pedolith](#) thickness at the toe-slope position (NAPED30) is 80 to 110 cm. In
926 the N-facing mid-slope position the [pedolith](#) thickness ranges from 60 to 110 cm.
927 [Pedolith](#) thicknesses based on GPR envelopes are generally thicker than [pedolith](#)
928 thicknesses observed in the field and do also not agree well with thicknesses based
929 on GPR profiles. The application of GPR envelopes to determine [pedolith](#)

Deleted: along

Deleted: soil

Deleted: soil

Deleted: Even so

Deleted: soil

Deleted: soil

Deleted: soil

Deleted: Supplementary Fig.

Deleted: soil

Deleted: Supplementary Fig.

Deleted: soil

954 thicknesses needs to be treated with care in this setting. On the contrary, GPR
955 profiles display rather continuous reflections that might represent interfaces within
956 the [pedolith](#), and could therefore be used to extrapolate point-scale ground-truth
957 information over the profile scale.

Deleted: soil

958

959 **5.3 Changes of [pedolith](#) thickness with hillslope position, aspect, and** 960 **latitude**

Deleted: soil

961 The [pedolith](#) thickness imaged with GPR envelopes over hillslope transects
962 reflect mainly physical properties, but also chemical properties (e.g., CIA, τ). This
963 approach gives the opportunity to study non-invasively possible changes in [pedolith](#)
964 thickness over hillslope position, aspect, and latitude ([Figs 12 to 15](#); [Figs S14 to S24](#);
965 Table 2). Here we summarize any regional trends in [pedolith](#) thickness between the
966 four study areas and different aspect (N- vs. S-facing) hillslopes (Fig. 2).

Deleted: soil

Deleted: soil

Deleted: Fig.

Deleted: Fig.

Deleted: soil

967 [Pedolith](#) thickness in a catena that develop under comparable climate and on
968 similar lithologies are expected to increase downhill (e.g., Birkeland, 1999). From
969 the top- to toe-slope position along a catena the potential for physical erosion
970 decreases downslope due to decreasing physical potential whereas the potential for
971 deposition increases. In Pan de Azúcar, the [pedolith](#) thickness based on the GPR
972 envelopes in the S-facing hillslope are constant, whereas the N-facing hillslope
973 indicates [pedolith](#) thickness increasing from top- to toe-slope. The possible slight
974 increase in [pedolith](#) thickness from top- to toe-slope can be explained by low
975 denudation rates due to very low precipitation rates in Pan de Azúcar. In Santa
976 Gracia, the constantly thin [pedoliths](#) at the S-facing top-slope are in contrast to the
977 thicker and more variable [pedolith](#) thickness in the mid-slope position. Bernhard et
978 al., (2018) describe an increase of the A to BC horizon from top- to toe-slope in the
979 S-facing hillslope. In Santa Gracia, precipitation and minor vegetation cover may
980 cause the increase of the [pedolith](#) thickness downslope as well as the variable
981 [pedolith](#) thickness in the mid-slope position. In La Campana, the [pedolith](#) thickness
982 based on GPR envelopes is highly variable. Bernhard et al., (2018) [also](#) observed
983 the thickest [pedolith](#) in the mid-slope position, [and](#) describe a disturbed hillslope

Deleted: Soil

Deleted: soil

Deleted: soil

Deleted: soil

Deleted: soils

Deleted: soil

Deleted: soil

Deleted: soil

Deleted: soil

Deleted: soil also

1001 with recent erosion events (e.g., possibly due to a past fire and temporary
1002 mobilization of sediment). Therefore, the S-facing hillslope in La Campana is a
1003 disturbed system and thus it is difficult to laterally extrapolate horizons. Due to the
1004 differences in pedolith thickness information from the different methods, pedolith
1005 thickness changes in hillslopes from Nahuelbuta are not further considered.

Deleted: therefore

Deleted: soil

Deleted: soil

1006 In the southern hemisphere, N-facing hillslopes are expected to be slightly warmer
1007 (higher solar irradiation) and drier (due to higher evaporation) than S-facing hillslope
1008 (e.g., Anderson et al., 2013). These differences in available regolith moisture could
1009 potentially lead to different vegetation and pedolith thickness. In Pan de Azúcar, the
1010 pedolith thickness of the S- and N-facing mid-slope positions cannot be attributed
1011 to differences in vegetation cover because it is absent from both the N- and S-facing
1012 slopes. In Santa Gracia, however, the thicker pedolith in the S-facing mid-slope
1013 position than in N-facing position can be attributed either to higher vegetation cover
1014 in the S-facing position (e.g., Riebe et al., 2017) or subtle lithological changes (e.g.

Deleted: the

Deleted: hillslope is

Deleted: the

Deleted: soil

Deleted: soil

Deleted: soil

Deleted: soil

Deleted: either

1015 Oeser et al., 2018). Different vegetation on S-facing and N-facing slope positions in
1016 La Campana could explain the higher variability in thickness in the S-facing mid-
1017 slope positions (35 to 70 cm) than the N-facing hillslope (50 to 60 cm). However,
1018 the aspect-related differences in La Campana may represent local heterogeneities
1019 (e.g., physical erosion) rather than a hillslope aspect-related trend (Bernhard et al.,
1020 2018). Finally, in Nahuelbuta, the GPR envelopes indicate highly variable, but also
1021 slightly thicker pedolith thickness in the S-facing than the N-facing hillslopes. A
1022 higher clay content in the S-facing than the N-facing hillslope is attributed to a more
1023 intense pedolith formation in the S-facing hillslope (Bernhard et al., 2018).
1024 Differences in pedolith thickness on S- and N-facing hillslopes increase from north
1025 to south in latitude due to the increasing difference of solar irradiation on
1026 evaporation, vegetation, and possible frost cracking (e.g., Riebe et al., 2017).

Deleted: soil

Deleted: soil

Deleted: soil

Deleted: soil

Deleted: are increasing

Deleted: N

Deleted: S

Deleted: soil

Deleted: due to

Deleted: due to the

Deleted: Soil

Deleted: N

Deleted: S

Deleted: due to

Deleted: N

Deleted: S

Deleted: in

1027 Not only is there a change in pedolith thickness with aspect, but also with latitude.
1028 Pedolith thickness increases and is more variable from north to south in latitude
1029 because of different climate and biota in each study area. Increasing precipitation
1030 rates from north to south allow an increase in cover and diversity of vegetation. From

1059 north to south pedoliths increase in thickness and are more variable in thickness
1060 due to the influence of biota (e.g., trees, burrowing animals). The increase in biota
1061 not only causes variable pedolith thickness, but also homogenizes pedoliths by
1062 bioturbation (e.g., Schaller et al., 2018). In addition, the increase in vegetation under
1063 increasing precipitation rates causes stabilization of hillslopes (e.g., Langbein and
1064 Schumm, 1958; Schmid et al., 2019; Starke et al., 2020). Hillslope denudation rates
1065 derived from in situ-produced cosmogenic nuclides increase from Pan de Azúcar to
1066 La Campana and slightly decrease for Nahuelbuta (Schaller et al., 2018; Oeser et
1067 al., 2018). Increasing pedolith thickness generally diminishes pedolith production
1068 rates (e.g., Heimsath et al., 1997) which under steady-state conditions equal
1069 hillslope denudation rates.

Deleted: N

Deleted: S in latitude, soils

Deleted: soil

Deleted: soils

Deleted: due to increasing precipitation rates

Deleted: form

Deleted: soil

Deleted: soil

1070

1071 5.4 Comparison to previous work and study caveats

1072 Geophysical studies focusing on the critical zone are a relatively new topic and
1073 have gained emphasis in the past decades (e.g., Parsekian et al., 2001). The results
1074 presented in this study complement a range of previous studies. Previous studies
1075 have used near surface geophysical methods to non-invasively measure subsurface
1076 properties and structures of the regolith and help to characterize critical zone related
1077 processes in the shallow subsurface (e.g., Scott and Pain, 2009). In this study, we
1078 focused in particular on deploying surface ground penetrating radar (GPR). The
1079 electromagnetic properties of the subsurface affect the propagation (i.e. velocity),
1080 attenuation (i.e. the energy loss), and reflectivity of the electromagnetic waves (e.g.,
1081 Jol, 2009). The electromagnetic wave velocity and attenuation can be linked to the
1082 dielectric permittivity and electrical conductivity of the subsurface, respectively.
1083 Previous work provides examples of environments, where GPR is suitable for
1084 mapping subsurface properties. These include karst areas, where structures in the
1085 regolith have been identified up to the bedrock interface (e.g., Estrada-Medina et
1086 al., 2010; Fernandes Jr. et al., 2015; Carriere et al., 2013), volcanic environments
1087 (e.g., Gomez et al., 2012; Ettinger et al., 2014), and dry environments (e.g., Bristow
1088 et al., 2007; Harari, 1996) as generally these regimes are characterized by low clay

1097 [and water content. The primary new contribution of this study with respect to existing](#)
1098 [regolith studies is the comparison of geophysical data to a wide range of physical](#)
1099 [and chemical properties that are commonly interpreted in projects studying surface](#)
1100 [processes.](#)

1101 [Previous work has highlighted the primary factors that GPR data can be sensitive](#)
1102 [to, and we briefly discuss these in the context of caveats associated with our work.](#)
1103 [Important factors that influence GPR data are the presence of water, solute content,](#)
1104 [and conductive materials such as clay \(e.g., Scott and Pain, 2009; Huisman et al.,](#)
1105 [2003\). In particular, clay as a highly conductive material has a significant impact on](#)
1106 [GPR signal as it affects the permittivity and the electrical conductivity at the same](#)
1107 [time \(e.g., Daniels, 2004\). With increasing amounts of clay in the subsurface, the](#)
1108 [signal penetrating is decreased due the increased attenuation of the waves.](#)
1109 [However, this behavior can be used to identify fine material in the subsurface, since](#)
1110 [in GPR profiles clay layers could be identified starting from spatial differences in](#)
1111 [signal penetration \(e.g., Gómez-Ortiz et al., 2010; De Benedetto et al., 2010; Tosti](#)
1112 [et al., 2013\). Furthermore, particle size beyond just clay abundance also plays a](#)
1113 [major role in GPR measurements, as the closer the particle size is to the wavelength](#)
1114 [of the emitted electromagnetic waves, the stronger are the reflections generated by](#)
1115 [these particles that can be seen in the detected signals \(e.g., Jol, 2009\). In this](#)
1116 [study, we incorporated clay content into our PCA and correlation analysis to identify](#)
1117 [if, and by how much, it may influence GPR observations.](#)

1118 [Previous studies have also documented how mineralogical variations with depth](#)
1119 [influence GPR signals. For example, the presence of minerals such as iron and](#)
1120 [aluminum oxides/hydroxides can play an important role in limiting the depth of](#)
1121 [penetration for GPR waves \(e.g., Čeru et al., 2018\) as iron-oxides have been linked](#)
1122 [with variations of relative permittivity, which might have in turn a considerable effect](#)
1123 [in the propagation of the GPR signals and effect the interpretation \(e.g., Van Dam](#)
1124 [et al., 2002; Van Dam and Schlager, 2000; Havholm et al., 2003\). Other studies](#)
1125 [showed that with increasing mafic mineral content in the subsurface, GPR signal](#)
1126 [attenuation is higher \(e.g., Breiner et al., 2011\). The presence of clay lenses in the](#)

1127 [regolith, alongside the layering, can influence the preferential flow path for regolith](#)
1128 [water, which can enhance reflectivity of the surfaces and therefore produce](#)
1129 [detectable reflections \(e.g., Zhang et al., 2014\). In this study, mineralogical](#)
1130 [variations with depth in the pedons were not available for comparison to our GPR](#)
1131 [data. However, we note that many of the processes described above may be](#)
1132 [responsible for the subsurface reflectors observed in Figures 12 to 15, and the fairly](#)
1133 [uniform granitoid composition of the different study areas means that mineralogical](#)
1134 [variations along any given hillslope profile are likely minimal and not a dominant](#)
1135 [source of signal in our GPR data.](#)

1136 [While the presence of volumetric water limits signal penetration, with an](#)
1137 [increasing effect for higher frequencies \(e.g., Utsi, 2017; Miller et al., 2002\), GPR](#)
1138 [has been more frequently used in the past two decades as a tool to detect water](#)
1139 [content variations in the subsurface as it has a strong effect on the dielectric](#)
1140 [permittivity \(e.g., Klotzsche et al., 2018\). In compact regoliths, where the volumetric](#)
1141 [water content is small, it has been shown that the bulk density has an important](#)
1142 [effect on the wave velocity, which is positively correlated \(Wang et al., 2016\). When](#)
1143 [solutes are present in the groundwater, the electrical conductivity of the medium](#)
1144 [increases, generating more signal loss, and therefore increasing wave attenuation](#)
1145 [\(e.g., Benedetto and Palewski, 2015\). One shortcoming of this study is that no](#)
1146 [independent information about subsurface water content was available for](#)
1147 [comparison to GPR observations as we did with the regolith physical and chemical](#)
1148 [properties. The depth varying chemical weathering indices we present \(e.g. CIA,](#)
1149 [Tau, Fig. 4 to 10\) would not be expected to correlate with present-day water content](#)
1150 [as these weathering indices developed over the timescale of regolith development](#)
1151 [\(millennia and longer\). Nevertheless, present-day water content would be expected](#)
1152 [to influence the GPR signals interpreted in this study, particularly in the more humid](#)
1153 [southern two study areas, and to a lesser or insignificant degree in the semiarid to](#)
1154 [arid northern two study areas. As a result, the subsurface correlations between the](#)
1155 [GPR envelopes and physical or chemical properties are likely influenced, to an](#)
1156 [unknown degree, by regolith moisture. The exclusion of regolith moisture data in our](#)

1157 [analysis may very well be a reason why we are not able to explain the full radar](#)
1158 [signature. Although without the inclusion of this data, peaks in the radar envelopes](#)
1159 [were still interpretable when compared to available physical and chemical property](#)
1160 [variations with depth. Thus, although the inclusion of regolith moisture data would](#)
1161 [be preferred, the omission of it does not negate the observed signals we were able](#)
1162 [to interpret.](#)

1163 [In locations, where the aforementioned regolith properties are not dominant, GPR](#)
1164 [can be used as a tool to identify structures and layering in both sediments \(e.g.,](#)
1165 [Bristow and Jol, 2003\) and regoliths, where interfaces ranging from the regolith-](#)
1166 [bedrock limit to the B horizon have been identified due to changes in the dielectric](#)
1167 [permittivity \(e.g., Yoder et al., 2001; Lambot et al., 2006\). In particular Zhang et al.](#)
1168 [\(2018\) showed the potential of mapping regolith layering in grasslands obtaining](#)
1169 [differences between GPR reflections and real regolith layer depth within 3 cm. In](#)
1170 [many situations, the interplay between different regolith properties make it difficult](#)
1171 [to understand the subsurface architecture without validation through regolith](#)
1172 [samples, as shown by Orlando et al. \(2016\) in the Rio Icacos watershed \(Puerto](#)
1173 [Rico\), where the stress regime, climate, and lithology are controlling the structures](#)
1174 [visible in GPR profiles. In comparing the previous studies to this one, we note that](#)
1175 [‘in general’ the results of this study were able to identify subsurface regolith structure](#)
1176 [and explain them, in many cases, with available physical and chemical properties.](#)
1177 [However, the complexity in GPR signals observed necessitates having pedons for](#)
1178 [local calibration when comparing to regolith weathering indices.](#)

1179

1180 **6 Conclusions**

1181 [Pedolith](#) thickness and properties are investigated in four study areas along a
1182 climate and vegetation gradient. The visually observed transition from [the](#) mobile
1183 [pedolith](#) to immobile [saprolite](#) coincides with one or more changes in measured
1184 physical and chemical properties in each study area. These physical and chemical
1185 properties in turn, influence return signals generated by Ground Penetrating Radar

Formatted: Indent: First line: 0"

Deleted: Soil

Deleted: soil

Deleted: saprolite

Deleted: -

1190 (GPR) in the [regolith](#), but no systematic trend is visible for which physical or
1191 chemical properties correlate with GPR based observations of [pedolith](#) thickness.
1192 Given this, the measurements and interpretation of GPR signals for systematically
1193 identifying subsurface changes in physical and chemical properties is not
1194 straightforward and differs for each study area. In general, the better developed the
1195 [pedolith](#) the better the correlation of GPR signals from point locations with physical
1196 and chemical [regolith](#) properties. We note that [choosing the GPR antenna frequency](#)
1197 [that is best suited for identifying \[pedolith\]\(#\) thickness is difficult, and calibration to local](#)
1198 [point locations \(e.g., pedons\) is always required. \[In general, we found the higher-\]\(#\)](#)
1199 [frequency \(1000 Mhz\) antenna to work best for imaging \[pedolith layers\]\(#\) and](#)
1200 [comparison to geochemical indicators in the arid and semi-arid study areas \(Pan de](#)
1201 [Azuár and Santa Gracia\). In contrast, the lower frequency antenna \(500 Mhz\)](#)
1202 [worked better in the Mediterranean and temperate study areas \(La Campana and](#)
1203 [Nahuelbuta\) for imaging \[pedolith structure and for comparison to geochemical\]\(#\)](#)
1204 [observations.](#)

Deleted: sub-surface

Deleted: soil

Deleted: soil

Deleted: soil

Deleted: what frequency

Deleted: soil

Deleted: .

Deleted: However, after local calibration between GPR signals...

Deleted: point locations is conducted, information of soil thickness from point locations can be up-scaled to hillslope transects with care.

1206 **Acknowledgement**

1207 We would like to thank CONAF and all the Park Rangers for the possibility of working
1208 in the natural parks, for providing access to the sample locations, and help inside
1209 the National Parks. [We also thank C. Pain and L. Worrall for their reviews of an](#)
1210 [earlier version of the manuscript.](#) We acknowledge support from the German
1211 Science Foundation (DFG) priority research program SPP-1803 "EarthShape: Earth
1212 Surface Shaping by Biota" (grants KR 3725/1-1, SCHA 1690/3-1, [and EH329/17-2](#)).
1213 RD was supported by a DFG Emmy Noether grant (DR 822/3-1).

Deleted: sub

Deleted: and

1214
1215
1216
1217

1232 **References:**

- 1233 Abdi, H., and Williams, L.J. Principal component analysis, Wiley interdisciplinary
1234 reviews: computational statistics 2, 433-459, 2010.
- 1235 Anderson, S.P., Anderson, S.P., and Tucker, G.E. Rock damage and regolith
1236 transport by frost: An example of climate modulation of the geomorphology of
1237 the critical zone, Earth Surface Processes and Landforms, DOI:
1238 10.1002/esp.3330, 2013.
- 1239 Aranha, P.R.A., Augustin, C.H.R.R., and Sobreira, F.G. The use of GPR for
1240 characterizing underground weathered profiles in the sub-humid tropics, Journal
1241 of Applied Geophysics, 49, 195-210, 2002.
- 1242 [Ardekani, M.R., Neyt, X., Benedetto, D., Slob, E., Wesemael, B., Bogaert, P.,
1243 Craeye, C., and Lambot, S. Soil moisture variability effect on GPR data,
1244 Proceedings of the 15th International Conference on Ground Penetrating
1245 Radar, Brussels, 214-217, doi: 10.1109/ICGPR.2014.6970416, 2014.](#)
- 1246 Armesto, J.J., Vidiella, P.E., and Gutierrez, J.R. Plant communities of the fog-free
1247 coastal desert of Chile: plant strategies in a fluctuating environment, Revista
1248 Chilena de Historia Natural, 66, 271-282, 1993.
- 1249 [Benedetto, A., and Pajewski, L. Civil engineering applications of ground penetrating
1250 radar, Springer, 2015.](#)
- 1251 Bernhard, N., Moskwa, L.-M., Oeser, R., von Blanckenburg, F., Boy, H., Brucker,
1252 E., Dippold, M., Ehlers, T.A., Fuentes-Espoz J.P., Godoy, R., Köster, M., Osses,
1253 P., Paulino, L., Schaller, M., Scholten, T., Seguel, O., Spielvogel, S., Spohn, M.,
1254 Stock, S., Stroncik, N., Uebnickel, K., Wagner, D., Kühn, P.: Pedogenic and
1255 microbial interrelations to regional climate and local topography: New insights
1256 from a climate gradient (arid to humid) along the Coastal Cordillera of Chile,
1257 Catena, 170, 335-355, 2018.
- 1258 Birkeland, P.W. Soils and Geomorphology, Oxford University Press, New York,
1259 1999.
- 1260 Braun, J.-J., Descloitres, M., Riotte, J., Fleury, S., Barbiero, L., Boeglin, J.-L.,
1261 Violette, A., Lacarce, E., Ruiz, L., Sekhar, M., Mohan Kumar, M.S.,
1262 Subramanian, S., and Dupre, B. Regolith mass balance inferred from combined
1263 mineralogical, geochemical and geophysical studies: Mule Hole gneissic
1264 watershed, South India, Geochimica et Cosmochimica Acta, 73, 935-961, 2009.
- 1265 [Breiner, J.M., Doolittle J.A., Horton R., and Graham R.C. Performance of ground-
1266 penetrating radar on granitic regoliths with different mineral composition, Soil
1267 Science, 176, 435-440, 2011.](#)
- 1268 Brimhall, G.H., and Dietrich, W.E. Constitutive mass balance relations between
1269 chemical composition, volume, density, porosity, and strain in metasomatic
1270 hydrochemical systems: Results on weathering and pedogenesis, Geochimica
1271 et Cosmochimica Acta, 51 (3), 567-587, 1987.
- 1272 Brimhall, G.H., Alpers, C., and Cunningham, A.B. Analysis of supergene ore-forming
1273 processes using mass balance principles, Economic Geology, 80, 1227-1254,
1274 1985.

Formatted: Line spacing: single

Formatted: Line spacing: single

Formatted: Line spacing: single

Formatted: Normal (Web), Indent: Left: 0", Hanging: 0.25", Line spacing: single

1275 [Bristow, C.S., and Jol, H.M. An introduction to ground penetrating radar \(GPR\) in](#)
1276 [sediments, Geological Society, London, Special Publications 211, 1, 1-7, 2003.](#)
1277 [Bristow, C.S., Jones, B.G., Nanson, G.C., Hollands, C., Coleman, M., and Price,](#)
1278 [D.M. GPR surveys of vegetated linear dune stratigraphy in central Australia:](#)
1279 [Evidence for linear dune extension with vertical and lateral accretion, Special](#)
1280 [Papers- Geological Society of America, 432, 19, 2017.](#)
1281 Bro, R., and Smilde, A.K. Principal component analysis, Analytical Methods, 6,
1282 2812-2831, 2014.
1283 [Carriere, S.D., Chalikakis, K., Senechal, G., Danquigny C., and Emblanch C.](#)
1284 [Combining electrical resistivity tomography and ground penetrating radar to](#)
1285 [study geological structuring of karst unsaturated zone, Journal of Applied](#)
1286 [Geophysics, 94, 31-41, 2013.](#)
1287 [Ceru, T., Dolonec, M., and Gosar, A. Application of Ground Penetrating Radar](#)
1288 [Supported by Mineralogical-Geochemical Methods for Mapping Unroofed Cave](#)
1289 [Sediments, Remote Sensing 10, 4, 639, 2018.](#)
1290 Chadwick, O.A., Brimhall, G.H., and Hendricks, D.M. From a black to a gray box - a
1291 mass balance interpretation of pedogenesis, Geomorphology, 3, 369-390,
1292 1990.
1293 Dal Bo, I., Klotzsche, A., Schaller, M., Ehlers, A.T., Kaufmann, M.S., Fuentes-
1294 Espoz, J.P., Vereecken, H., van der Kruk, J. Geophysical imaging of regolith in
1295 landscapes along a climate and vegetation gradient in the Chilean Coastal
1296 Cordillera, Catena, 180, 146-159, 2019.
1297 [Daniels, D.J. Ground penetrating radar, IEE Radar, Sonar, Navigation and Avionics](#)
1298 [Series, The Institution of Electrical Engineers, 15, 2001.](#)
1299 [De Benedetto, D., Castrignano, A., Sollitto, D., and Modugno, F. Spatial relationship](#)
1300 [between clay content and geophysical data, Clay Minerals 45, 2, 197-207, 2010.](#)
1301 De Coster, A., and Lambot, S. Fusion of Multifrequency GPR Data Freed From
1302 Antenna Effects, Journal of Selected Topics in Applied Earth Observations and
1303 Remote Sensing, 11 (2), 664-674, 2018.
1304 Doolittle, J.A., and Collins, M.E. Use of soil information to determine application of
1305 ground penetrating radar. Journal of Applied Geophysics, 33 (1-3), 101-105,
1306 1995.
1307 Doolittle, J.A., Minzenmayer, F.E., Waltman, F.W., Benham, E.C., Tuttle, J.W., and
1308 Peaslee, S.D. Ground-penetrating radar soil suitability map of the conterminous
1309 United States, Geoderma, 141, 416-421, 2007.
1310 [Estrada-Medina, H., Tuttle, W., Graham, R.C., Allen, M.F., and Jimenez-Osornio, J.](#)
1311 [Identification of Underground Karst Features using Ground-Penetrating Radar in](#)
1312 [Northern Yucatan, Mexico, Vadose Zone Journal, 9, 3, 653-661, 2010.](#)
1313 [Ettinger, S., Manville, V., Kruse, S., and Paris, R. GPR-derived architecture of a](#)
1314 [labor-generated fan at Cotopaxi volcano, Ecuador, Geomorphology, 213, 225-](#)
1315 [239, 2014.](#)
1316 [Fernandes Jr., A.L. Medeiros, W.E., Bezerra, F.H.R., Oliveira Jr., J.G., and Cazarin,](#)
1317 [C.L. GPR investigation of karst guided by comparison with outcrop and](#)

Formatted: Line spacing: single

Formatted: Font color: Auto

Formatted: Line spacing: single

Formatted: Line spacing: single

1318 [unmanned aerial vehicle imagery](#), *Journal of Applied Geophysics*, 112, 268-278,
1319 [2015](#).

1320 Gerber, R., Felix-Henningsen, P., Behrens, T., and Scholten, T. Applicability of
1321 ground-penetrating rader as a tool for nondestructive soil-depth mapping on
1322 Pleistocene slope deposits, *Journal of Plant Nutrition and Soil Science*, 173 (2),
1323 173-184, 2010.

1324 [Gomez, C., Kataoka, K.S., and Tanaka, K. Large-scale internal structure of the
1325 Sambongi Fan-Towada Volcano, Japan: Putting the theory to the test using PGR
1326 on volcanoclastic deposits](#), *Journal of volcanology and geothermal research*,
1327 229, 44-49, 2012.

1328 [Gomez-Ortiz, D., Martin-Crespo, T., Martin-Velazquez, S., Martinez-Pegan, P.,
1329 Higuera, H., and Manzana, M. Application of ground penetrating radar \(GPR\)
1330 to delineate clay layers in wetlands. A case study in the Soto Grande and Soto
1331 Chico watercourses, Donana \(SW Soain\)](#), *Journal of Applied Geophysics*, 72, 2,
1332 107-113, 2010.

1333 Green, A.G. Applications of 3-D georadar methods to diverse environmental and
1334 engineering problems, *Progress in Environmental and Engineering Geophysics*,
1335 edited by Chao, C. and Jianghai, X., Science Press USA, 220-226, 2004.

1336 Guo, L., Chen, J., Cui, X., Fan, B., and Lin, H. Application of ground penetrating
1337 radar for coarse root detection and quantification: a review, *Plant Soil*, 362, 1-
1338 23, 2013.

1339 Guo, L., Mount, G.J, Hudson, S., Lin, H., and Levia, D. Pairing geophysical
1340 techniques helps understanding of the near-surfce Critical Zone: Visualization
1341 of preferential rouging of stemflow along coarse roots. *Geoderma*, 357, 113953,
1342 2020.

1343 [Harari, Z. Ground-penetrating radar \(GPR\) for imaging stratigraphic features and
1344 groundwater in sand dunes](#), *Journal of Applied Geophysics*, 36, 1, 43-52, 1996/
1345 [Havholm, K.G., Bergstrom, N.D., Jol, H.M., and Running, G.L. GPR survey of a
1346 Holocene aeolian/fluviol/lacustrine succession, Lauder Sandhills, Manitoba,
1347 Canada](#), *Geological Society, London, Special Publication 211*, 47-54, 2003.

1348 Heimsath, A.M., Dietrich, W.E., Nishiizumi, K., and Finkel, R.C. The soil
1349 productionfunction and landscape equilibitium, *Nature*, 388, 358-361, 1997.

1350 Heimsath, A.M., Dietrich, W.E., Nishiizumi, K., and Finkel, R.C. Cosmogenic
1351 nuclides, topography, and the spatial variation of soil depth, *Geomorphology*,
1352 27, 151-172, 1999.

1353 Hilgard, E.W. *Soils: Their Formation, Properties, Compositions and Relations to
1354 Climate and Plant Growth in the Humid and Arid Regions*, The Macmillan
1355 Company, New York, 1914.

1356 Holbrook, W.S., Riebe, C.S., Elwaseif, M., Hayes, J.L., Vasler-Reeder, K., Harry,
1357 D.L., Malazian, A., Dosseto, A., Hartsough, P.C., and Hopmans, W.
1358 Geophysical constraints on deep weathering and water storage potential in the
1359 Southern Sierra Critical Zone Observatory. *Earth Surface Processes and
1360 Landforms*, 39, 366-380, 2014.

Formatted: Line spacing: single

Formatted: Normal, Indent: Left: 0", Hanging: 0.25", Line spacing: single

Formatted: Line spacing: single

Formatted: Line spacing: single

1361 Hruska, J., Cermak, J., and Sustek, S. Mapping tree root system with ground-
1362 penetrating radar. *Tree Physiology*, 19, 125-130, 1999.

1363 [Huisman, J.A., Hubbard, S.S., Annan, P.A. Measuring soil water content with](#)
1364 [ground penetrating radar: A review, *Vadose Zone Journal*, 2, 476-491,](#)
1365 [doi:10.2136/vzj2003.4760](#), 2003.

1366 [IUSS Working Group WRB. World reference base for soil resources 2014, update](#)
1367 [2015. Prepared by Schad P, van Huyssteen C, Micheli E. 192 pp. *World Soil*](#)
1368 [Resources Reports No. 106, FAO, Rome. 2015.](#)

1369 Jenny, H. *Factors of Soil Formation: A System of Quantitative Pedology*, Dover
1370 Publications, New York, 1994.

1371 Jol, H.M. (Ed.): *Ground penetrating radar: theory and applications*, Elsevier Science,
1372 Amsterdam, the Netherlands ; Oxford, United Kingdom, 2009.

1373 Kassambara, A. *Practical guide to cluster analysis in R: unsupervised machine*
1374 *learning*, STHDA, 2017.

1375 [Klotzsche, A, Jonard, F., Looms, M.C., van der Kruk, J., and Huisman, J.A.](#)
1376 [Measuring soil water content with ground penetrating radar: A decade of](#)
1377 [progress, *Vadose Zone Journal*, 17, 1, 1-9, 2018.](#)

1378 [Lambot, S., Antoine, M., Vanclooster, M., Slob E.C. Effect of soil roughness on the](#)
1379 [inversion of off-ground monostatic GPR signal for noninvasive quantification of](#)
1380 [soil properties, *Water Resources Research*, 42, 3, 2006.](#)

1381 Langbein, W.B., and Schumm, S.A. Yield of sediment in relation to mean annual
1382 precipitation, *Transaction American Geophysical Union*, 39, 1076-1084, 1958.

1383 Liu, J.L., and Marfurt, K.J. Instantaneous Spectral Attributes to Detect Channels,
1384 *Geophysics*, 72, 23-31.
1385 <http://dx.doi.org/10.1190/1.2428268>, 2007.

1386 Mellett, J.S. Ground penetrating radar applications in engineering, environmental
1387 management, and geology, *Journal of Applied Geophysics*, 33 (1-3), 157-166,
1388 1995.

1389 Miller, T.W., Hendrickx, J.M.H., and Borchers, B. Radar detection of buried
1390 landmines field soils. *Vadose Zone Journal*, 3 (4). 1116-1127, 2002.

1391 Mutz, S.G., Ehlers, T.A., Werner, M., Lehmann, G., Stepanek, C., and Li, J. Where
1392 is Late Cenozoic climate change most likely to impact denudation?, *Earth*
1393 *Surface Dynamics*, 6, 271-301, <https://doi.org/10.5194/esurf-2017-47>, 2018.

1394 [Oeser, R.A., Stroncik, N., Moskwa, L.-M., Bernhard, N., Schaller, M., Canessa, R.,](#)
1395 [van der B Rin, L., Köster, M., Brucker, E., Stock, S.S., Fuentes, J.P., Godoy, R.,](#)
1396 [Matus, F.J., Osés Pedraza, R., Osés McIntyre, P., Paulino, L., Seguel, O.,](#)
1397 [Bader, M.Y., Boy, J., Dippold, M.A., Ehlers, T.a., Kühn, P., Kuzyakiv, Y.,](#)
1398 [Peinweber, P., Scholten, T., Spielvogel, S., Spohn, M., Üubernickel, K.,](#)
1399 [Tielbörger, K., Wagner, D., and von Blanckenburg, F. Chemistry and](#)
1400 [microbiology of the Critical Zone along a steep climate and vegetation gradient](#)
1401 [in the Chilean Coastal Cordillera, *Ctena*, 170, 183-203, 2018.](#)

1402 [Orlando, J., Comas, Z., Hynek, S., Buss, H.L., and Brantley, S.L. Architecture of the](#)
1403 [deep critical zone in the Rio Icacos watershed \(Luquillo Critical Zone](#)

Formatted: Line spacing: single

Formatted: Line spacing: single

Formatted: English (US)

1404 [Observatory, Puerto Rico\) inferred from drilling and ground penetrating radar](#)
1405 [\(GPR\), *Earth Surface Processes and Landforms*, 41, 13, 1823-1840, 2016.](#)

1406 Parsekian, A.D., Singha, K., Minsley, B.J., Holbrook, W.S., and Slater, L. Multiscale
1407 geophysical imaging of the critical zone, *Reviews of Geophysics*, 53, 1-26,
1408 2015.

1409 Porder, S., Vitousek, M.P., Chadwick, O.A., Chamberlain, C. P. and Hilley, G.E.
1410 Uplift, Erosion, and Phosphorous Limitation in Terrestrial Ecosystems,
1411 *Ecosystems*, 10, 158-170, 2007.

1412 Rabassa, J., and Clapperton, C.M. Quaternary glaciations of the southern Andes,
1413 *Quaternary Science Reviews*, 9, 153-174, 1990.

1414 Riebe, C.S., Hahm, W.J. and Brantley, S.L. Controls on deep critical zone
1415 architecture: a historical review and four testable hypothesis, *Earth Surface*
1416 *Processes and Landforms*, 42, 128-156, 2017.

1417 Roering, J.J., Kirchner, J.W., and Dietrich, W.E. Hillslope evolution by nonlinear,
1418 slope-dependent transport: Steady state morphology and equilibrium
1419 adjustment timescales, *Journal of Geophysical Research*, 106, B8, 16499-
1420 16513. 2001.

1421 Roering, J.J., Marshall, J., Booth, A.M., Mort, M., and Jin, Q. Evidence for biotic
1422 controls on topography and soil production, *Earth and Planetary Science*
1423 *Letters*, 289, 183-190, 2010.

1424 Saarenketo, T. Electrical properties of water in clay and silty soils. *Journal of Applied*
1425 *Geophysics*, 40, 73-88, 1998.

1426 Sarkar, R., Paul, K.B., and Higgins, T.R. Impacts of soil physiochemical properties
1427 and temporal-seasonal soil-environmental status on ground-penetrating radar
1428 response. *Soil Science Society of America Journal*, 83, 542-554, 2019.

1429 Scarpone, C., Schmidt, M.G., Bulmer, C.E., and Knudby, A. Modelling soil thickness
1430 in the critical zone for Southern British Columbia, *Geoderma*, 282, 59-69, 2016.

1431 Schaller, M., Ehlers, T., Lang, K., Schmid, M., and Fuentes-Espoz, J. Addressing
1432 the contribution of climate and vegetation cover on hillslope denudation, Chilean
1433 Coastal Cordillera (26°–38° S), *Earth and Planetary Science Letters*, 489, 111-
1434 122, 2018.

1435 [Schmid, M., Ehlers, T.A., Werner, C., Hickler, T., and Fuentes-Espoz, J.-P. Effect](#)
1436 [of changing vegetation and precipitation on denudation – Part 2: Predicted](#)
1437 [landscape response to transient climate and vegetation cover over millennial to](#)
1438 [million-year timescales, *Earth Surface Dynamics*, 6\(4\), 859–881,](#)
1439 [doi:10.5194/esurf-6-859-2018, 2018.](#)

1440 [Scott K., and Pain, C. *Regolith science*, Csiro Publishing, 2009.](#)

1441 Sedgwick, P. Pearson's correlation coefficient, *BMJ*, 345:e4483, 2012.

1442 Starke, J., Ehlers, T.A., and Schaller, M. Latitudinal effect of vegetation on erosion
1443 rates identified along western South America. *Science*, 367, 1358-1361, 2020.

1444 [Steelman, C.M., Endres, A.L., and Jones, J.P. High-resolution ground-penetrating](#)
1445 [radar monitoring of soil moisture dynamics: Field results, interpretation, and](#)
1446 [comparison with unsaturated flow model. *Water Resour. Res.* 48, W09538,](#)
1447 [doi:10.1029/2011WR011414, 2012.](#)

Formatted: Line spacing: single

Deleted: and Granger, D. Quantifying deep and near-surface chemical erosion on cosmogenic nuclides in soils, saprolite, and sediment, *Earth Surface Processes and Landforms*, 38, 523-533, 2013.†
Riebe, C.S.,

Formatted: Line spacing: single

1453 Sucre, E.B., Tuttle, J.W., and Fox, T.R. The use of ground-penetrating radar to
 1454 accurately estimate soil depth in rocky forest soils. *Forest Science* 57 (1), 59-
 1455 66, 2011.

1456 Telford, W.M., Geldart, L.P., Sheriff, R.E. and Keys, D.A. (Eds.): *Applied*
 1457 *Geophysics*, 2th Edition, Cambridge University Press, Cambridge, 770.
 1458 <http://dx.doi.org/10.1017/CBO9781139167932>, 1990.

1459 Tosti, F., Patriarca, C., Slob, E., Benedetto, A., and Lambot, S. Clay content
 1460 evaluation in soils through GPR signal processing. *Journal of Applied*
 1461 *Geophysics*, 97, 69-80, 2013.

1462 [Utsi, E.C. Ground penetrating radar: theory and practice, Butterworth-Heinemann,](#)
 1463 [2017.](#)

1464 [van Dam, R.L., and Schlager, W. Identifying causes of ground-penetrating radar](#)
 1465 [reflections using time-domain reflectometry and sedimentological analyses,](#)
 1466 [Sedimentology, 47, 435–449, doi: 10.1046/j.1365-3091.2000.00304.x. 2000.](#)

1467 [van Dam, R.L., Nichol, S.L., Augustinus, P.C., Parnell, K.E., Hosking, P.L., and](#)
 1468 [McLean, R.F. GPR stratigraphy of a large active dune on Paren-garenga](#)
 1469 [Sandspit, New Zealand, The Leading Edge, 22, 865–881, 2003.](#)

1470 [Wang, P., Hu, Z., Zhao, Y., and Li, X. Experimental study of soil compaction effects](#)
 1471 [on GPR signals, Journal of Applied Geophysics, 126m 128-137, 2016.](#)

1472 Wei, T. Package 'corrplot'-Visualization of a correlation matrix. v0.60. cran. rproject.
 1473 org, 2012.

1474 Werner, C., Schmid, M., Ehelrs, T.A., Fuentes-Espoz, J.P., Steinkamp, J., Forrest,
 1475 M., Liakka, J., Maldonado, A., and Hickler, T. Effect of changing vegetation and
 1476 precipitation on denudation - Part1; Predicted vegetation composition and cover
 1477 over the last 21 thousand years along the Coastal Cordillera of Chile, *Earth*
 1478 *Surface Dynamics*, 6, 829-858, <https://doi.org/10.5194/esurf-6-829-2018>, 2018.

1479 Wold, S., Esbensen, K., and Geladi, P. Principal component analysis,
 1480 *Chemometrics and intelligent laboratory systems*, 2, 37-52, 1987.

1481 [Yoder, R.E., Freeland, R.S., Ammons, J.T., and Leonard, L.L. Mapping agricultural](#)
 1482 [fields with GPR and EMI to identify offsite movement of agrochemicals, Journal](#)
 1483 [of Applied Geophysics, 47, 3-4, 251-259, 2001.](#)

1484 Zhang, J., Lin, H., and Doolittle, J. Soil layering and preferential flow impacts on
 1485 seasonal changes of GPR signals in two contrasting soils. [Geoderman](#), 213,
 1486 560-569, 2014.

1487 [Zhang, X., Dao, L., Zhang, C., Morrison, L., Hong, B., Zhang H., and Gan, Y.](#)
 1488 [Mapping the spatial distribution of soil depth in a grassland ecosystem with the](#)
 1489 [aid of ground penetrating radar and GIS \(Northwestern Sichuan, China\),](#)
 1490 [Grassland Science, 64, 4, 217-225, 2018.](#)

Formatted: Line spacing: single

Formatted: Line spacing: single

Formatted: Line spacing: single

Deleted: geoderman

Deleted: ¶

Formatted: Line spacing: single

Formatted: Font color: Text 1

1496 **Figure captions**

1497 Fig. 1:

1498 Digital elevation model (Data source: GTOPO30) for the Chilean Coastal Cordillera
1499 and the Central Andes showing the four investigated study areas (from [north](#) to
1500 [south](#)): Pan de Azúcar (~26° S); Santa Gracia (~30° S); La Campana (~33° S); and
1501 Nahuelbuta (~38° S).

Deleted: N

Deleted: S

1502

1503 Fig. 2:

1504 Satellite images (Data source: Google Earth©) of the four study areas from N to S
1505 in latitude: A) Pan de Azúcar; B) Santa Gracia; C) La Campana; and D) Nahuelbuta.
1506 Red stars indicate the pedon positions whereas the blue lines represent the
1507 locations of the geophysical investigations.

1508

1509 Fig. 3:

1510 N- and S-facing hillslopes of the four study areas with locations of pedons and
1511 transects of ground penetrating radar indicated by the red double arrows. [For
1512 complete characterization and interpretation of the pedons see Fig. 2 in Bernhard
1513 et al. \(2018\) and Figs 3 to 6 in Oeser et al. \(2018\).](#)

Deleted: soil

Formatted: Indent: Left: -0"

1514

1515 Fig. 4:

1516 Compilation of physical and chemical investigations with depth at the pedon location
1517 in the mid-slope position of the S-facing hillslope in Pan de Azúcar. Properties
1518 shown are: 1) GPR transect and the envelope profile of the 500 MHz measurement;
1519 2) GPR transect and the envelope profile of the 1000 MHz measurement; 3) Bulk
1520 density; 4) Grain size distribution of sand, silt, and clay; 5) Loss on ignition LOI; 6)
1521 Chemical index of alteration CIA; 7) Chemical index of the mass transfer coefficient
1522 Tau τ ; and 8) volumetric strain ϵ_{strain} . The black line indicates the boundary between
1523 the mobile [pedolith](#) and the immobile [saprolioth](#) (after Oeser et al., 2018) and the gray
1524 area with green lines reflects the transition zone from B to C horizon (after Bernhard
1525 et al., 2018).

Deleted: soil

Deleted: saprolite

1531
1532 Fig. 5:
1533 Primary component analysis PCA of properties for all four pedons in Pan de Azúcar.
1534 A) Scree plot showing the percentage of explained variances and B) Variables -
1535 PCA.
1536
1537 Fig. 6:
1538 Compilation of physical and chemical investigations at the pedon location in the mid-
1539 slope position of the S-facing hillslope in Santa Gracia. Properties shown are listed
1540 in caption of Fig. 4.
1541
1542 Fig. 7:
1543 Primary component analysis PCA of properties for all four pedons in Santa Gracia.
1544
1545 Fig. 8:
1546 Compilation of physical and chemical investigations at the pedon location in the mid-
1547 slope position of the S-facing hillslope in La Campana. Properties shown are listed
1548 in in caption of Fig. 4.
1549
1550 Fig. 9:
1551 Primary component analysis PCA of properties for all four pedons in La Campana.
1552
1553 Fig. 10
1554 Compilation of physical and chemical investigations at the pedon location in the mid-
1555 slope position of the S-facing hillslope in Nahuelbuta. Properties shown are listed
1556 as in caption of Fig. 4. Note that only the 500 MHz signal and envelope profile exist.
1557
1558 Fig. 11:
1559 Primary component analysis PCA of properties for all four pedons in Nahuelbuta.
1560

Deleted: ¶
Fig. 5:¶

Moved (insertion) [2]

Formatted: Justified, Line spacing: 1.5 lines

Deleted: soil

Deleted: soil

Deleted: soil

Deleted: soil

1567 Fig. 12:
1568 A) 1000 MHz GPR transect and B) envelope for the S-facing hillslope in Pan de
1569 Azúcar. The hillslope transect spans over ~20 m and includes pedon AZPED60,
1570 AZPED50, and AZPED40 (black boxes). The potential [pedolith](#) thickness based on
1571 the envelopes is indicated by stars (in B). The red bar indicates the B to C horizon
1572 transition as given in Bernhard et al. (2018). Uphill is from left to right. Note that in
1573 the radar data the air wave and background removal is applied.

Deleted: soil

1574
1575 Fig. 13:
1576 1000 MHz GPR signal and envelope for the mid-slope position of the S-facing
1577 hillslope position in Santa Gracia (SGPED40). The hillslope transect spans over ~20
1578 m. Interpretation of the radar signal are indicated where possible (stippled lines in A
1579 and B). The potential [pedolith](#) thickness is indicated based on the envelope profile.
1580 Uphill is from left to right. Lines and symbols in figures as described in Fig. 12.

Deleted: soil

1581
1582 Fig. 14:
1583 500 MHz GPR signal and envelope for the mid-slope position of the S-facing
1584 hillslope in La Campana (LCPED20). The hillslope transect spans over ~8 m.
1585 Interpretation of the radar signal are indicated where possible (stippled and black
1586 lines in A and B). The potential [pedolith](#) thickness is indicated based on the envelope
1587 profile. Uphill is from left to right. Lines and symbols in figures as described in Fig.
1588 12.

Deleted: soil

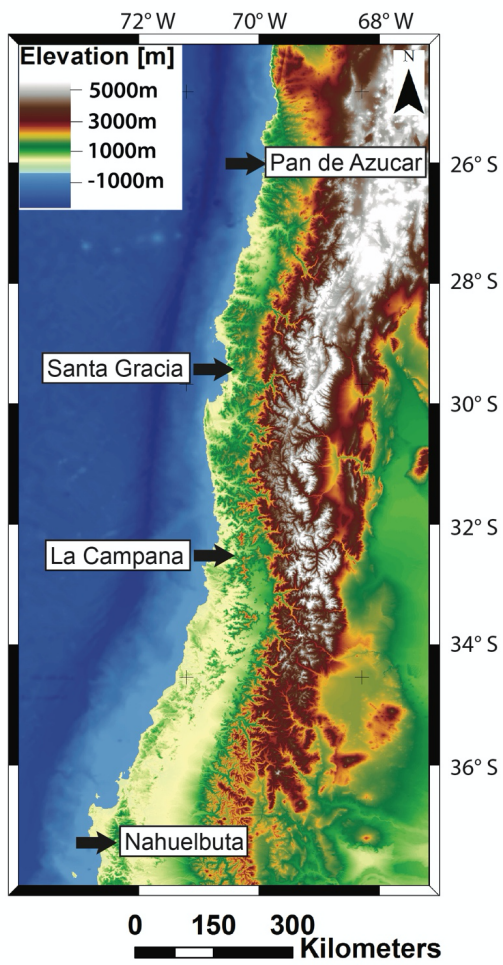
1589
1590 Fig. 15:
1591 500 MHz GPR signal and envelope for the mid-slope position of the S-facing
1592 hillslope in Nahuelbuta (NAPED20). The hillslope transect spans over ~20 m.
1593 Interpretation of the radar signal are indicated where possible (stippled lines in A
1594 and B). The potential [pedolith](#) thickness is indicated based on the envelope profile.
1595 Uphill is from left to right. Lines and symbols in figures as described in Fig. 12.

Deleted: soil

1596

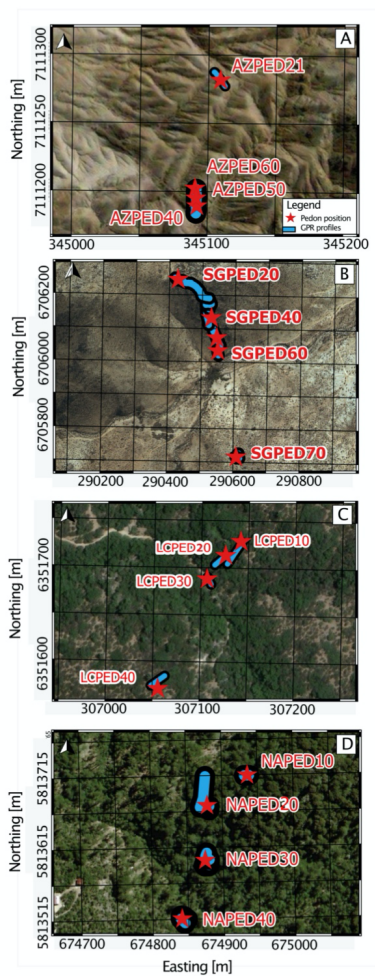
1601

1602 Fig. 1:



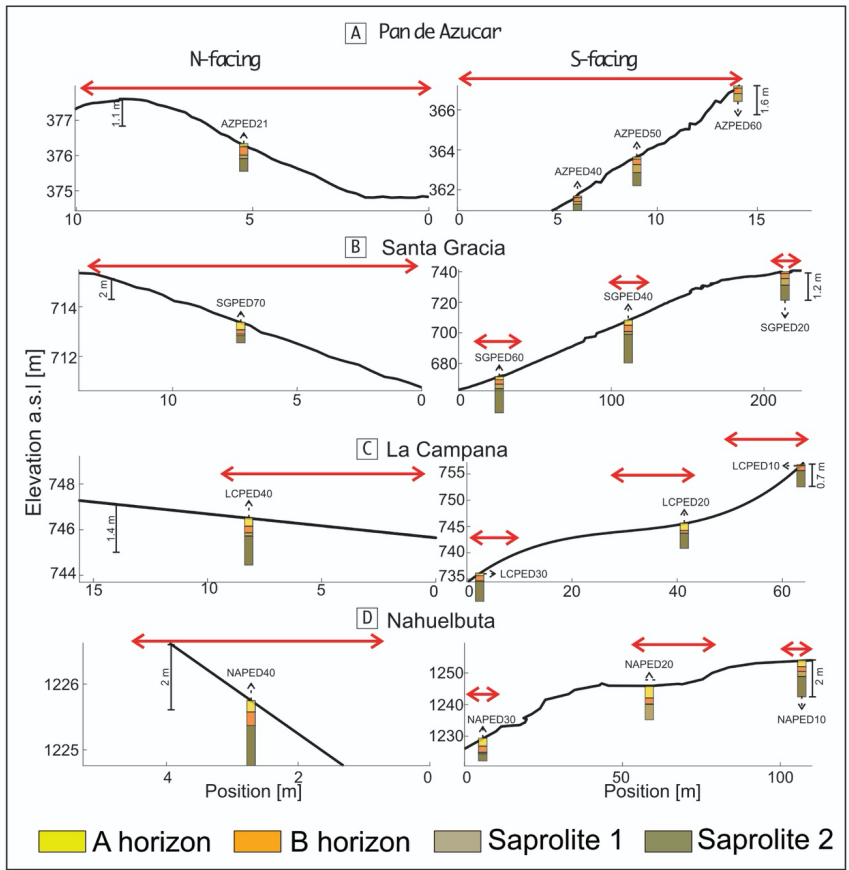
1603
1604

1605 Fig. 2:

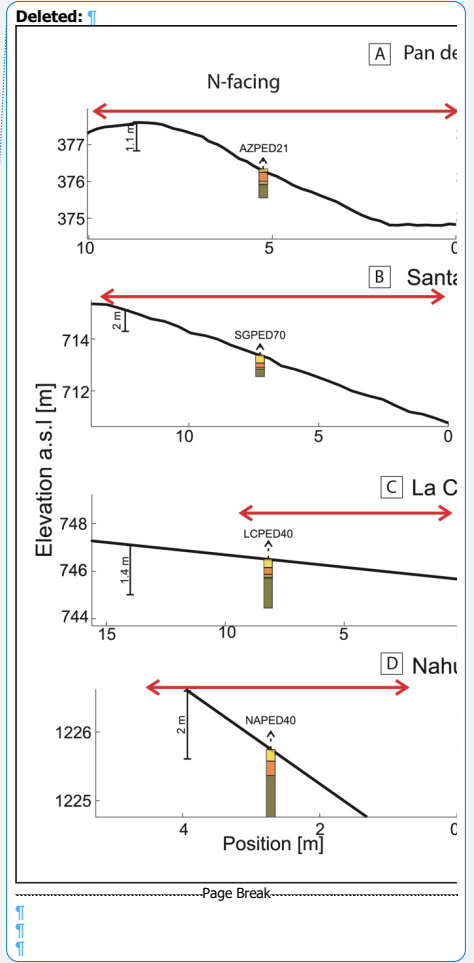


1606

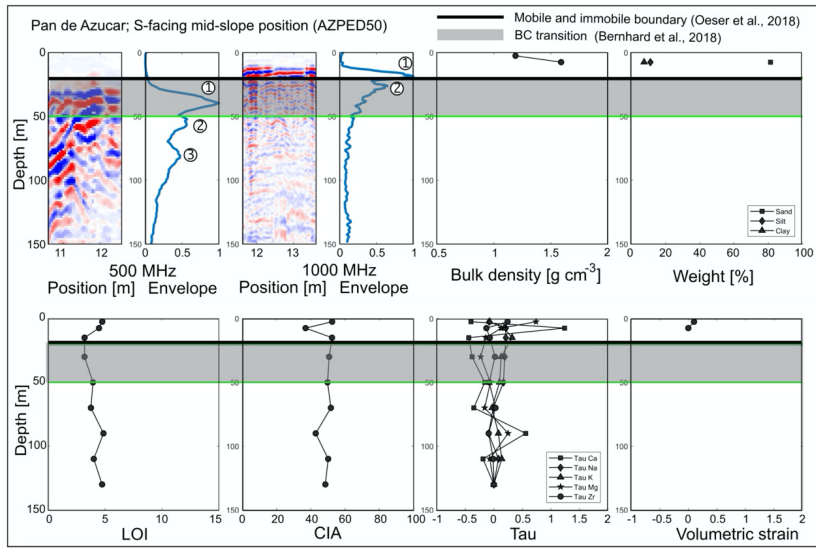
1607 Fig. 3:



1608
1609

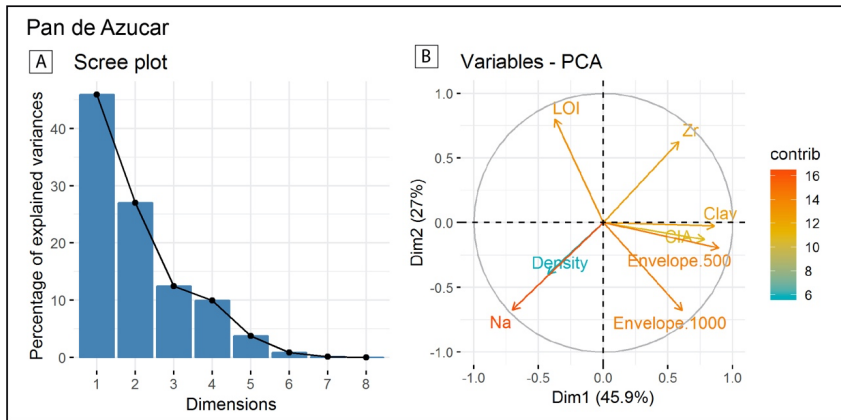


1616 Fig. 4:



1617
1618
1619
1620

Fig. 5:



1621
1622
1623

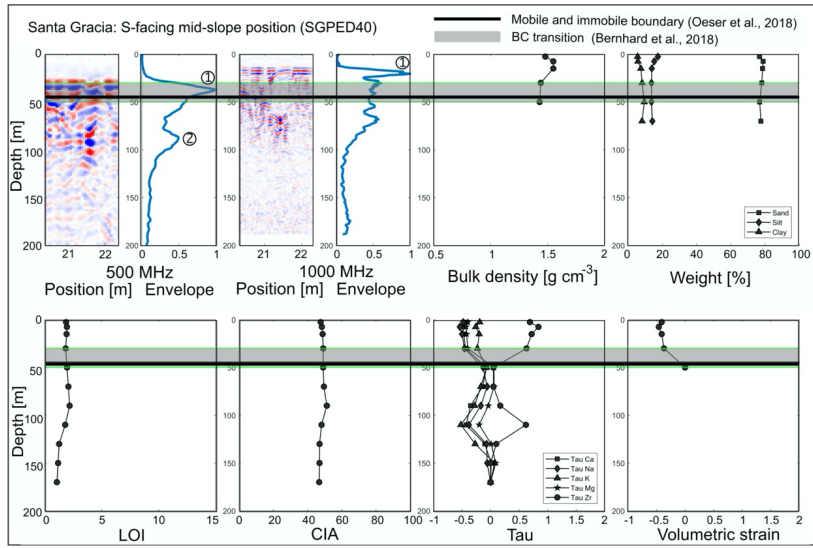
Deleted:

Moved up [2]: ¶
Fig. 5: ¶

Moved (insertion) [1]

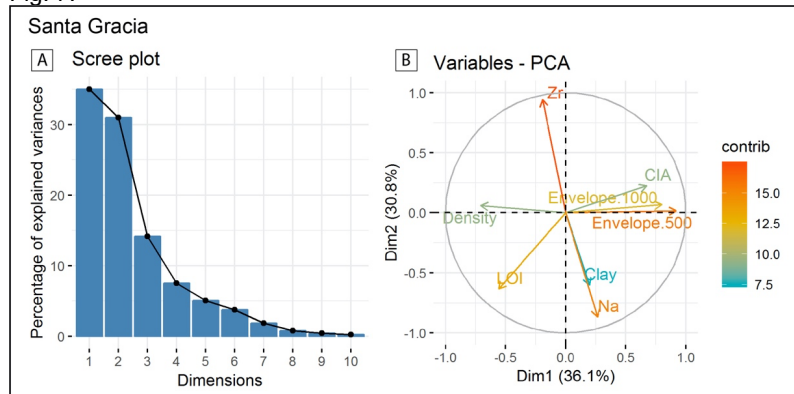
1627
1628

Fig. 6:

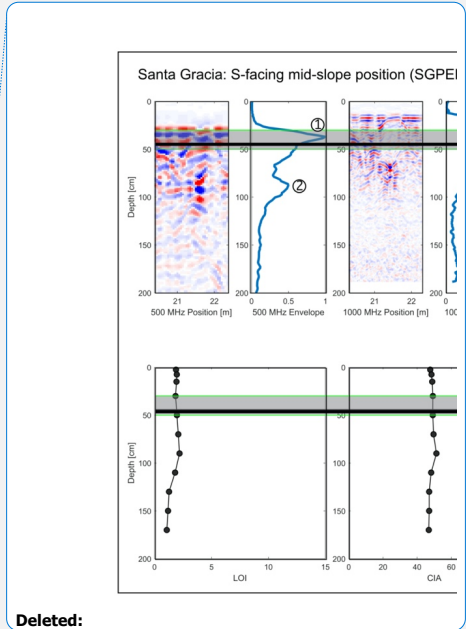


1629
1630
1631

Fig. 7:



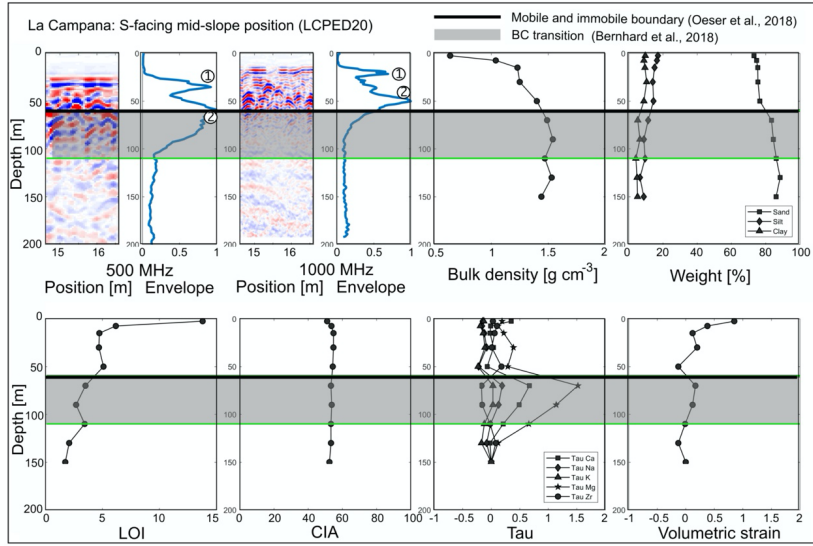
1632
1633
1634



Deleted:

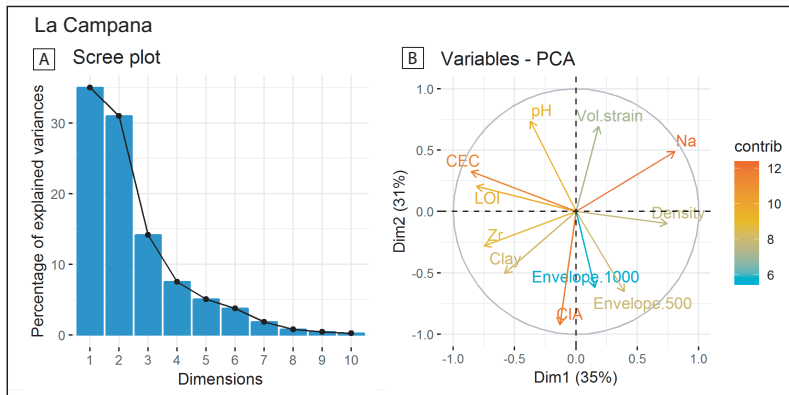
Deleted: ↑
↑

1638
1639 Fig. 8:

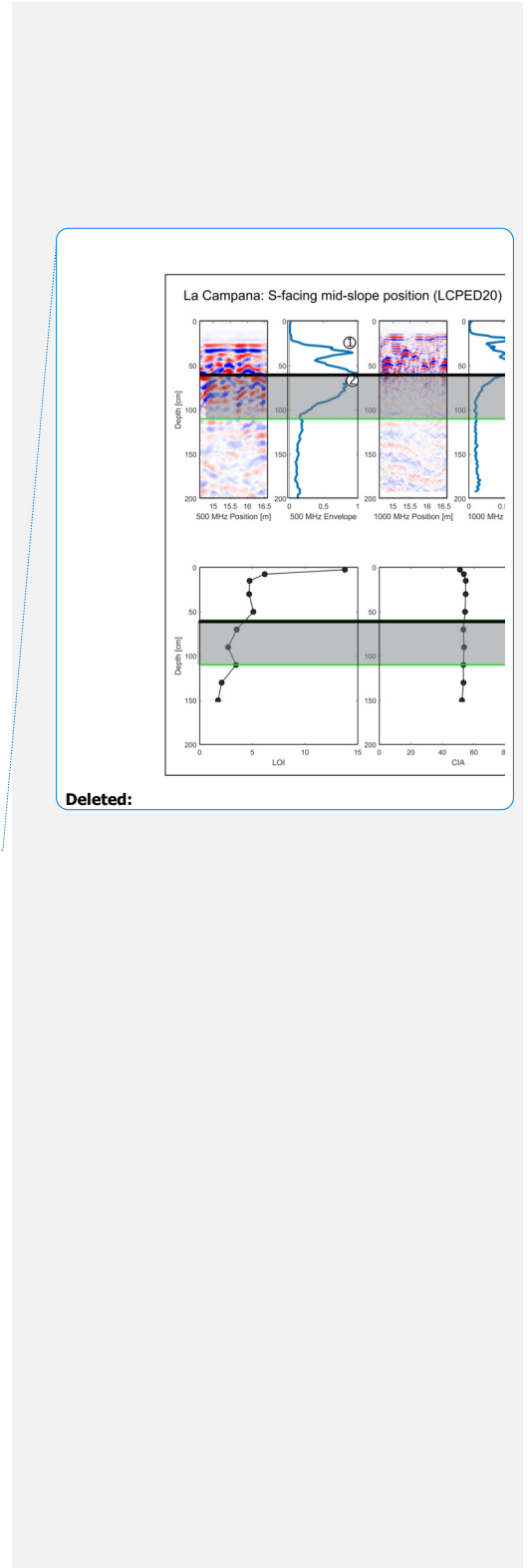


1640
1641
1642
1643

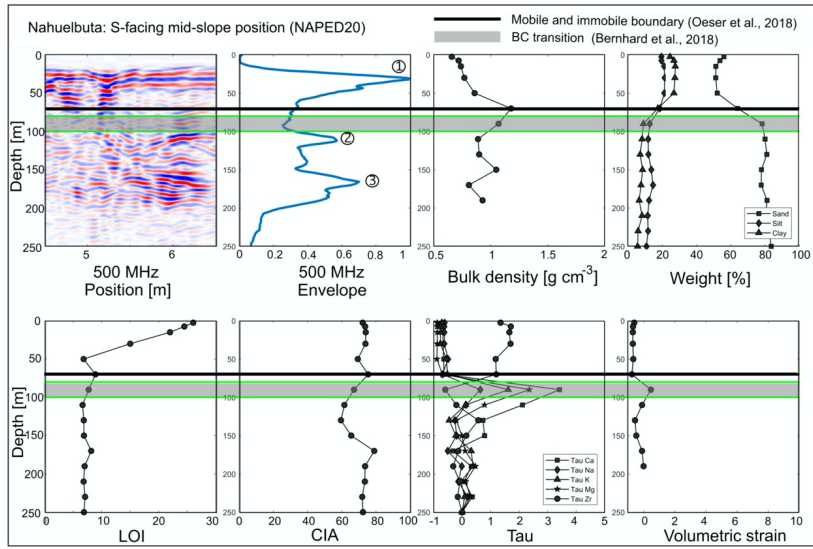
Fig. 9:



1644
1645

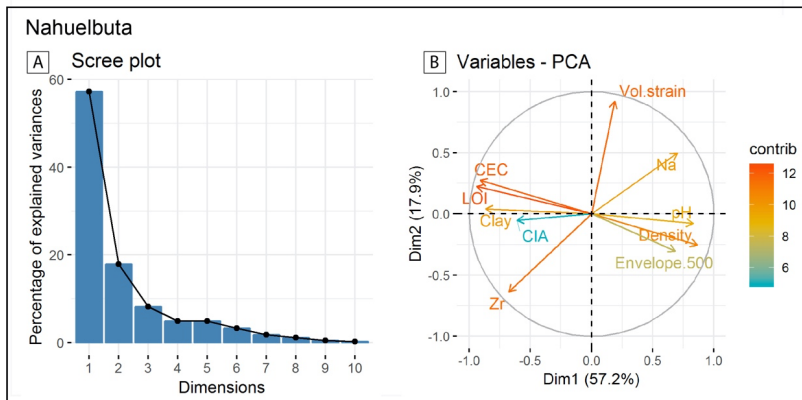


1647 Fig. 10:

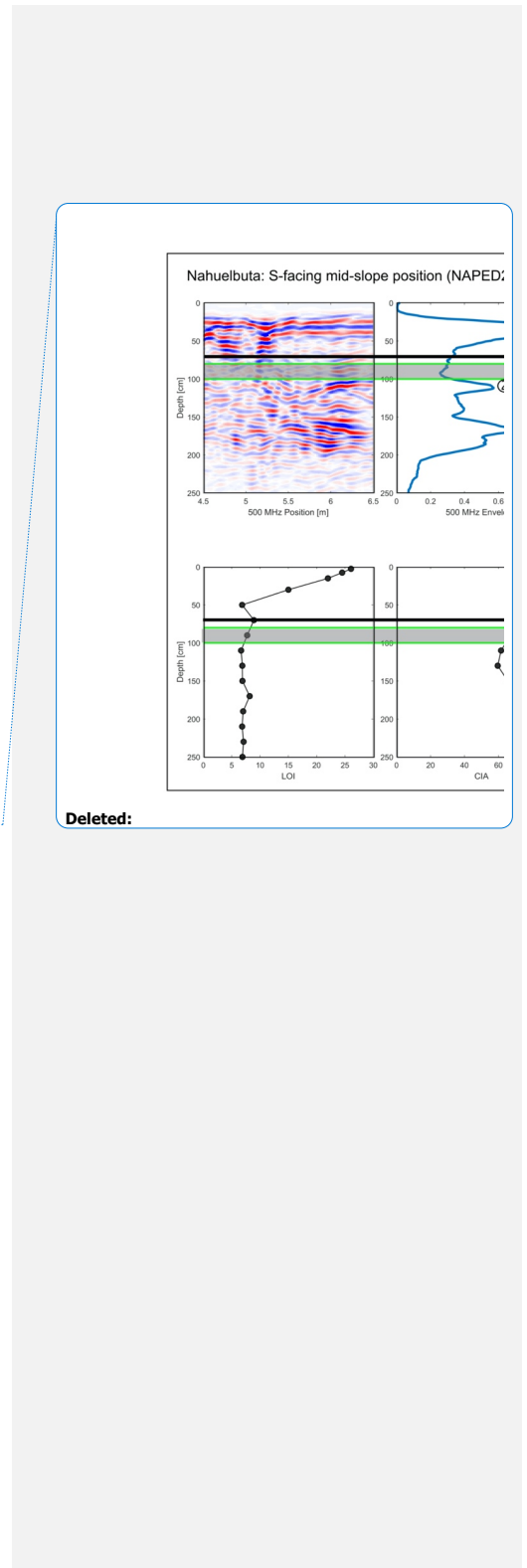


1648
1649
1650

Fig. 11:

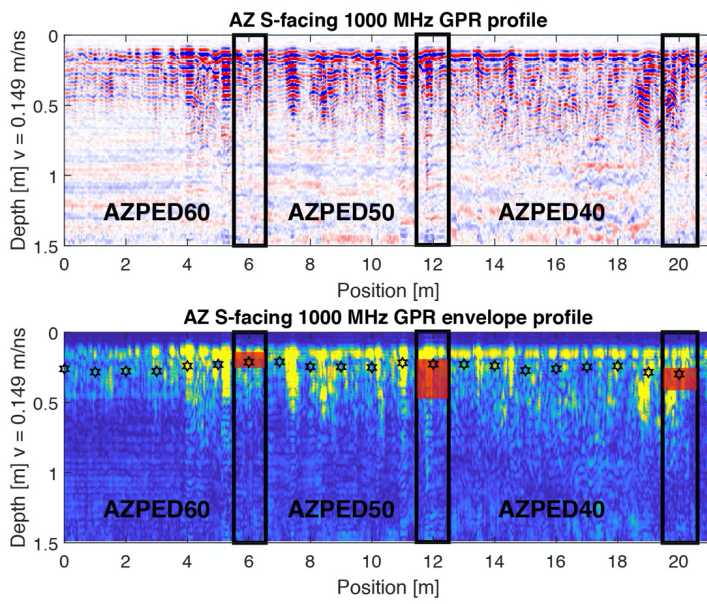


1651
1652
1653
1654



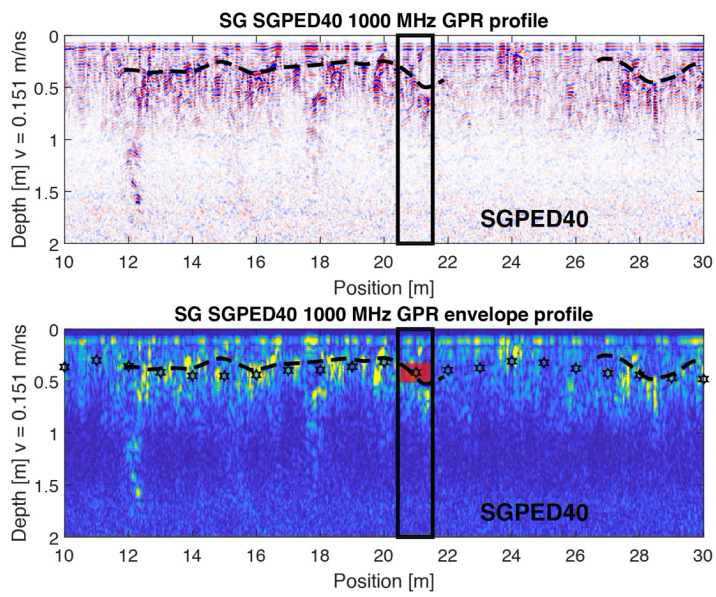
Deleted:

1656 Fig. 12:
1657



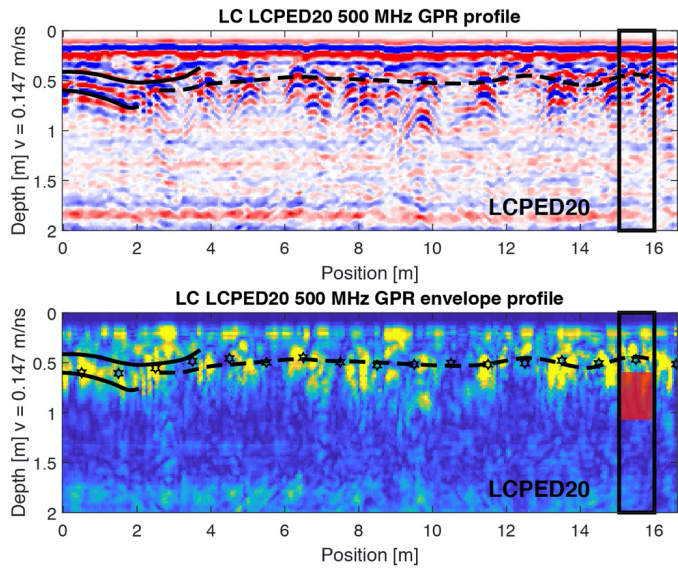
1658
1659
1660

1661 Fig. 13:



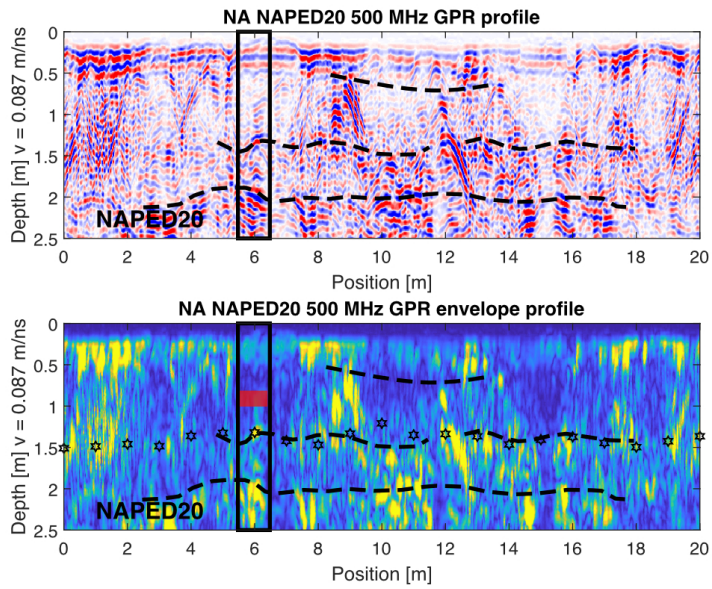
1662
1663

1664 Fig. 14:
1665



1666
1667
1668

1669 Fig. 15:
1670



1671
1672

1673
1674

Table 1:

Table 1: Overview of physical, chemical, and geophysical properties determined in the four different study areas				
Property	Abreviation	Units	Meaning	Reference
Pedolith bulk density	ρ_b	g/cm ³	Weight of unit volume	Bernhard et al., 2018
Grain size distribution	GSD	%	Weight percent of different grain sizes smaller than 2 mm	Bernhard et al., 2018
Potential hydrogene	pH		Acid and base properties	Bernhard et al., 2018
Cation exchange capacity	CEC	cmol/kg	Soil ability to hold positively charged ions	Bernhard et al., 2018
Loss on ignition	LOI	%	Loss of volatiles due to excessiv heating	Oeser et al., 2018
Chemical index of alteration	CIA		Degree of weathering	Oeser et al., 2018
Mass transfer coefficient	τ	m/s	Chemical gain or loss	Oeser et al., 2018
Volumetric strain	ϵ_{strain}		Volumetric gain or loss	Oeser et al., 2018
Electric permittivity	ϵ_r		Structural changes, porosity/soil water content	Dal Bo et al., 2019; This study
Electrical conductivity	σ	mS/m	Clay, salinity	Dal Bo et al., 2019; This study

1675
1676
1677
1678
1679
1680
1681
1682

Table 2:

Table 2: Data compilation for pedons in the investigated four study areas in the Chilean Coastal Cordillera															
Pedon	Location		Altitude m	Position	Aspect °	Slope °	Field observations				GPR point depth ⁽⁵⁾		GPR transect depth ⁽⁶⁾		
	°S	°W					BC-horizon transition ⁽¹⁾ cm	Mobile/Immob. ⁽²⁾ cm	Mobile/Immob. ⁽²⁾ cm	GPR ⁽⁴⁾ cm	500 MHz cm	1000 MHz cm	500 MHz cm	1000 MHz cm	
Pan de Azucar															
AZPED60	26.11012	70.54922	343	top	60	5	14-26		22	30-55 (?)	40	20/25/45			
AZPED50	26.11027	70.54922	333	mid	0	40	20-50	20	20-55	40/50/70	20/25/35/45				
AZPED40	26.11024	70.54921	326	toe	0	33	23-40		25	20-40	40/55	20/30			
AZPED21	26.10936	70.54907	342	mid	180	25	20-30	20	30-45	37/55/75	20/30/45/55	40 ± 2	28 ± 7		
Santa Gracia															
SGPED20	29.75636	71.16721	718	top	240	5	20-30		30	30	40	20/30/40/50	37 ± 5	34 ± 3	
SGPED40	29.75738	71.16635	682	mid	0	25	30-50	50	45	60	45/10/30/40/55/65	40 ± 7	36 ± 5		
SGPED60	29.75826	71.16615	638	toe	0	20	40-60		55	-	37/50	20/30	39 ± 7	35 ± 6	
SGPED70	29.76120	71.16559	690	mid	180	15	25	35	35	NA	40	20/30	35 ± 3	28 ± 2	
La Campana															
LCPED10	32.95581	71.06332	734	top	60	7	34		45	40/50	35/50/70/10/30/35/50/65	55 ± 6	44 ± 5		
LCPED20	32.95588	71.06355	718	mid	0	23	60-110	60	60	50/60	35/60/70	20/38/50	59 ± 6	45 ± 4	
LCPED30	32.95615	71.06380	708	toe	60	35	34-55		55	45/50	35/70	20/30/38	50 ± 9	41 ± 4	
LCPED40	32.95720	71.06425	724	mid	120	12	36-103	35	35	-	35/65	20/30/40	56 ± 6	47 ± 6	
Nahuelbuta															
NAPED10	37.80735	73.01285	1248	top	60	5	50-75		70	70/75	35/45/120	82 ± 15			
NAPED20	37.80770	73.01357	1239	mid	60	15	80-100	95	70	75/95	35/110/170	101 ± 8			
NAPED30	37.80838	73.01345	1228	toe	0	20	63-85		90	-	5/90/120/140	96 ± 6			
NAPED40	37.80904	73.01380	1200	mid	180	13	65-90	70	60	40/50	40/60/120	95 ± 11			

⁽¹⁾ Depth of BC-horizon transition from Bernhard et al., 2018
⁽²⁾ Depth of mobile pedolith from Schaller et al., 2018
⁽³⁾ Depth of mobile pedolith from Oeser et al., 2018
⁽⁴⁾ Depth based on data from Dal Bo et al., 2019
⁽⁵⁾ Depth based on single point GPR envelopes (This study)
⁽⁶⁾ Average depth based on envelopes from GPR transect data (This study)

1683
1684
1685
1686

Table 1: Overview of physical, chemical, and geophysical properties determined in the four different study areas		
Property	Abreviation	Units
Soil bulk density	ρ_b	g/cm ³
Grain size distribution	GSD	%
Potential hydrogene	pH	
Cation exchange capacity	CEC	cmol/kg
Loss on ignition	LOI	%
Chemical index of alteration	CIA	
Mass transfer coefficient	τ	m/s
Volumetric strain	ϵ_{strain}	
Electric permittivity	ϵ_r	
Electrical conductivity	σ	mS/m

Deleted:

Table 2: Data compilation for pedons in the investigated four study areas in the Chilean Coastal Cordillera															
Soil profile	Location		Altitude m	Position	Aspect °	Slope °	BC-horizon transition ⁽¹⁾ cm	Mobile/Immob. ⁽²⁾ cm	Mobile/Immob. ⁽²⁾ cm	GPR ⁽⁴⁾ cm	GPR point depth ⁽⁵⁾		GPR transect depth ⁽⁶⁾		
	°S	°W									500 MHz cm	1000 MHz cm	500 MHz cm	1000 MHz cm	
Pan de Azucar															
AZPED60	26.11012	70.54922	343	top	60	5	14-26		22	30-55 (?)	40	20/25/45			
AZPED50	26.11027	70.54922	333	mid	0	40	20-50	20	20-55	40/50/70	20/25/35/45				
AZPED40	26.11024	70.54921	326	toe	0	33	23-40		25	20-40	40/55	20/30			
AZPED21	26.10936	70.54907	342	mid	180	25	20-30	20	30-45	37/55/75	20/30/45/55	40 ± 2	28 ± 7		
Santa Gracia															
SGPED20	29.75636	71.16721	718	top	240	5	20-30		30	30	40	20/30/40/50	37 ± 5	34 ± 3	
SGPED40	29.75738	71.16635	682	mid	0	25	30-50	50	45	60	45/10/30/40/55/65	40 ± 7	36 ± 5		
SGPED60	29.75826	71.16615	638	toe	0	20	40-60		55	-	37/50	20/30	39 ± 7	35 ± 6	
SGPED70	29.76120	71.16559	690	mid	180	15	25	35	35	NA	40	20/30	35 ± 3	28 ± 2	
La Campana															
LCPED10	32.95581	71.06332	734	top	60	7	34		45	40/50	35/50/70/10/30/35/50/65	55 ± 6	44 ± 5		
LCPED20	32.95588	71.06355	718	mid	0	23	60-110	60	60	50/60	35/60/70	20/38/50	59 ± 6	45 ± 4	
LCPED30	32.95615	71.06380	708	toe	60	35	34-55		55	45/50	35/70	20/30/38	50 ± 9	41 ± 4	
LCPED40	32.95720	71.06425	724	mid	120	12	36-103	35	35	-	35/65	20/30/40	56 ± 6	47 ± 6	
Nahuelbuta															
NAPED10	37.80735	73.01285	1248	top	60	5	50-75		70	70/75	35/45/120	82 ± 15			
NAPED20	37.80770	73.01357	1239	mid	60	15	80-100	95	70	75/95	35/110/170	101 ± 8			
NAPED30	37.80838	73.01345	1228	toe	0	20	63-85		90	-	5/90/120/140	96 ± 6			
NAPED40	37.80904	73.01380	1200	mid	180	13	65-90	70	60	40/50	40/60/120	95 ± 11			

Deleted: